HHS Public Access

Author manuscript

Nat Chem Biol. Author manuscript; available in PMC 2024 February 07.

Published in final edited form as:

Nat Chem Biol. 2024 January ; 20(1): 52–61. doi:10.1038/s41589-023-01406-2.

Calcium-gated potassium channel blockade via membrane-facing fenestrations

Chen Fan[1], **Emelie Flood**[#,2], **Nattakan Sukomon**[#,1], **Shubhangi Agarwal**[1], **Toby W. Allen**[*,2], **Crina M. Nimigean**[*,1,3]

[1]Department of Anesthesiology, Weill Cornell Medicine, New York, USA.

[2]School of Science, RMIT University, Melbourne, Australia

[3]Departments of Physiology and Biophysics, Weill Cornell Medicine, New York, USA

Abstract

Quaternary ammonium blockers were previously shown to bind in the pore to block both open and closed conformations of large-conductance calcium-activated potassium (BK and MthK) channels. Since blocker entry was assumed through the intracellular entryway (bundle-crossing), closed-pore access suggested that the gate was not at the bundle-crossing. Since structures of closed MthK, a *Methanobacterium thermoautotrophicum* homolog of BK channels, revealed a tightly-constricted intracellular gate, we investigated the membrane-facing fenestrations as alternative pathways for blocker access directly from the membrane. Atomistic free-energy simulations showed that intracellular blockers indeed access the pore through the fenestrations and a mutant channel with narrower fenestrations displayed no closed-state TPeA block at concentrations that blocked WT. Apo BK channels display similar fenestrations, suggesting that blockers may use them as access paths into closed channels. Thus, membrane fenestrations represent a non-canonical pathway for selective targeting of specific channel conformations, opening novel ways to selectively drug BK channels.

Introduction

Potassium (K^+) channels play a central role in controlling selective ion conduction across cell membranes, forming the basis of electrical-osmotic balance and signaling in the nervous system[1]. Large-conductance calcium-activated K^+ (BK) channels are activated by both increases in intracellular calcium (Ca^{2+}) and membrane depolarization and regulate critical processes such as muscle contractility and neuronal excitability[1–3]. Changes in BK channel

[*]Corresponding authors: Crina M. Nimigean: crn2002@med.cornell.edu, Toby W. Allen: toby.allen@rmit.edu.au.

Chen Fan's current address: Science for Life Laboratory, Department of Biochemistry and Biophysics, Stockholm University, Solna, Sweden

Emelie Flood's current address: Schrödinger, Inc., 1540 Broadway, 24th floor, New York, NY 10036, United States

[#]Indicates the authors that contributed equally to the manuscript

Author contributions

CF, CN and TA designed the study. CF and SA prepared cryo-EM samples, collected and analyzed cryo-EM data. NS and CF performed mutant screening and stopped-flow assays and analyzed the data. EF and TA performed and analyzed the MD simulations. CF, CN, and TA assembled the manuscript and wrote the paper with input from all authors.

Competing interests statement

The authors declare no competing interests.

activity are associated with conditions such as hypertension, asthma, and neurological diseases[4]. However, despite major interest and research efforts, there is currently a paucity of FDA-approved selective BK channel pharmacological modulators[4]. Most compounds that target ion channels bind to or near their ion conduction pathway, which, due to its high conservation across channels, invariably leads to low selectivity. Consequently, discovery and investigation of novel, channel-specific sites that can be targeted by small molecules in a state-dependent fashion is critical for drug design.

Forays for novel sites for targeted therapeutics require structural information of multiple functional states. Structural evidence from single-particle cryo-electron microscopy (cryo-EM) is now available for BK[5–7] channels from different species, in apo and Ca^{2+}-bound conformations. However, while the Ca^{2+}-bound BK structures are most likely open, because of their wide-open intracellular pore entryway, it is less clear whether the Ca^{2+}-free structures represent closed conformations; the width of their intracellular gate is still large enough to allow a hydrated K^+ into the pore (Fig. 1b), which either indicates that the gate is elsewhere[8,9 10,11] or suggests existence of potential closed states for which structures have not yet been determined. On the other hand, structures of Ca^{2+}-free and Ca^{2+}-bound MthK, a prokaryotic homologue of BK channels that is only activated by Ca^{2+}, unambiguously represent open and closed states, respectively. The pore-lining TM2 helices of closed, Ca^{2+}-free MthK form a tight constriction at the intracellular bundle crossing, impenetrable to ions[12]. Ca^{2+} binding to the gating ring leads to a large outward swing of the TM2 helices (Fig. 1a), opening the intracellular gate widely, like in BK channels (Fig. 1b), to allow ions access to the pore[12].

Because BK and MthK channels are homologous, discovery of novel binding sites and state-dependent entry pathways for molecules in MthK can be directly applicable to eukaryotic BK channels. Their pores are highly conserved, with large cavities, wide intracellular pore entrances, and large unitary currents, unlike other K^+ channels[6,7,13–15]. They have conserved cytoplasmic domains that bind Ca^{2+} and undergo similar conformational rearrangements leading to channel opening[12,16–19]. Importantly, their ion conduction pathways are blocked in both open and closed states by quaternary ammonium (QA) compounds, unlike other related K^+ channels, which are only blocked in open states[10,11,20–22]. Finally, as we highlight in this work, both BK and MthK channels, display state-dependent membrane-facing entryways from membrane into the pore (fenestrations), not observed in other K^+ channels[5,12]. Although, unlike MthK, BK channels have voltage sensor domains, their disposition does not impede pore access through fenestrations.

QA compounds (blockers) have been used in ion channel research to learn about properties of channel pores as well as activation and inactivation gates[11,22–30]. In this work, we identified and characterized a novel, state-dependent pathway for QA molecules to enter the MthK pore and we discuss its conservation in eukaryotic BK channels. We searched for such pathway in MthK because, in contrast to our previous findings that QA molecules block closed MthK channels[21], our structure of closed MthK indicated a tightly shut intracellular gate, through which blockers cannot squeeze[12].

Here, we used single-particle cryo-EM, functional assays and fully-atomistic molecular dynamics (MD) simulations to show that the closed MthK channel pore can be accessed by QA blockers not via the canonical ion conduction pathway, but by partitioning into the lipid bilayer and entering the pore via membrane-exposed fenestrations[12]. These fenestrations are also observed in Ca^{2+}-free but not Ca^{2+}-bound BK channel structures[5–7] suggesting that they may constitute a viable path for blockers and related molecules to bind and enter the pore, and thus a novel target for specific BK channel inhibitor design. This alternative, non-canonical access of the closed pore by QA blockers via a path distinct from the ion conduction path, require reevaluation of previous proposals that MthK (and possibly BK) channels gate at the selectivity filter.

Results

TPeA and bbTBA bind below the selectivity filter in closed MthK

Previous functional fast-mixing stopped-flow fluorescence assays allowed direct measure of QA block of closed MthK channels, indicating that some QA molecules can access the closed pore[21]. Since entering the pore via the ion conduction pathway is not possible with a tightly shut intracellular gate[12], we searched for alternate access pathways.

To investigate if blockers bind closed MthK, we solved structures of purified Ca^{2+}-free closed MthK channels in lipid nanodiscs with 2 different QA blockers, TPeA (Tetrapentylammonium) and bbTBA (N-(4-[benzoyl]benzyl)-N,N,N-tributylammonium), via single-particle cryo-EM. The MthK-TPeA cryo-EM map (Extended Data Fig. 1, 2, Supplementary Table 1) revealed the cross-shaped TPeA density consistent with a planar four-fold symmetric molecule (Fig. 2) before imposing symmetry. The final map was constructed with 4-fold symmetry (3.5 Å, Extended Data Fig. 2, 3). The resolution of the MthK structure in complex with the non-symmetric bbTBA was 3.5 Å without symmetry (Extended Data Fig. 2, 3) with the blocker density below the selectivity filter (SF), in a similar location as TPeA (Fig. 2). Because the aromatic rings did not fit perfectly, we used MD flexible fitting (MDFF) with the structure relaxed in a membrane, which lead to an identical blocker binding pose (Supplementary Fig. 1). The locations of TPeA and bbTBA in closed MthK are consistent with QA blockers binding locations in KcsA[31,32] and open MthK[20] channels (Extended Data Fig. 4).

TPeA and bbTBA binding changes closed MthK pore conformation

The structures of MthK-TPeA and MthK-bbTBA are similar to the published MthK closed state[12], with several differences. First, unlike MthK[15] and other K^+ channels[33] that have 4 K^+ densities at defined SF binding sites (referred to as S1 to S4, from the extracellular side, Fig. 2e), the MthK-TPeA SF contains only one density, in S4, and the MthK-bbTBA contains densities only at the S3 and S4 sites (Fig. 2f–g). Second, the acyl chains of TPeA and the longer benzyl-benzyl moiety of bbTBA interact with residues I84 and F87, leading to a downward rearrangement of the F87 side chain compared with blocker-free closed MthK (Fig. 2h–i). The other three bbTBA acyl chains (4 carbons per arm) are shorter than those of TPeA (5 carbons per arm), and too far away to interact with the F87. This leads to a mix of F87 conformations in the final reconstruction of MthK bbTBA, where two of the

F87 side chains adopt an up and the other 2 a down conformation (Fig. 2j, Extended Data Fig. 1e). Both features have also been observed in structures of KcsA in complex with QA compounds[34] and were associated with SF inactivation[35,36].

Our previously-reported closed MthK structure[12] was of relatively low resolution (3.6 Å). We report here a new closed MthK structure (referred as blocker-free MthK) with higher resolution (3.1 Å) and improved SF density map (Extended Data Fig. 1, 2, Supplementary Table 1). The atomic model is identical to the previous structure[12] (RMSD= 0.3 Å for C_α and 0.8 Å for all atoms). The SF contains four densities in the S1–S4 sites and all F87 side chains are in the up conformation (Fig. 2e,h). All structural comparisons were performed relative to this higher-resolution blocker-free MthK structure.

Lipids bind to fenestrations of closed MthK

We reported previously the appearance of fenestrations at interfaces between adjacent subunits of the MthK tetramer, lined by TM2 helices, and located approximately halfway through the membrane, connecting the pore with the lipid bilayer in the closed channel (Fig. 3a)[12]. A similar fenestration exists also in Ca^{2+}-free BK channel structures (Extended Data Fig. 4 a, g)[7]. When the channels open, the large motions of the pore-lining TM2 helices that expand the intracellular gate, also obstruct these fenestrations (Fig. 3a–b, Extended Data Fig. 4 a–b)[12 7]. The MthK fenestrations are lined by hydrophobic residues, and a lipid density with one acyl chain penetrating through the fenestration half-way into the pore is observed, as predicted by MD simulations[12] (Fig. 3). Similar lipids observed in MthK-TPeA and MthK-bbTBA structures (Extended Data Fig. 1a–d) likely stabilize TPeA binding in the cavity via hydrophobic interactions between acyl chains, which can contribute to blocker binding equilibrium in the closed state (Fig. 3b). Since the lipid contribution to the blocker binding site is state-dependent, it may provide a basis for the higher binding affinity of TPeA for the closed compared to open MthK[21].

These fenestrations offer an alternative pathway for QA blockers to enter the pore of closed MthK channels directly from the membrane. TPeA and bbTBA qualitatively satisfy water/lipid permeability to enter membranes from the aqueous environment and bind within the water-filled cavity as they are amphipathic (positive charge and long hydrophobic acyl and aromatic chains make them both water and lipid soluble[37]) - as we demonstrate below with significant partitioning to the lipid-bilayer interface. They also match the size criteria to squeeze through the fenestrations (largest dimensions of TPeA and bbTBA are ~7 and ~10 Å, respectively). We next used MD to investigate whether these compounds can access the MthK closed pore via fenestrations.

Restricted blocker entry via the closed intracellular gate

We performed all-atom MD simulations of full-length closed MthK (Fig. 4a), to explore the entry pathway of intracellular TPeA. Unbiased flooding simulations of the channel with 50 mM TPeA revealed rapid partitioning of the blockers to the membrane interface, as well as to the intracellular gate entrance, but were unable to enter the pore during 4 μs of simulation (Extended Data Fig. 5a–b). We therefore turned to enhanced sampling simulations to study TPeA entry energetics.

We used Umbrella Sampling (US) simulations to calculate the free energy profile for TPeA to first enter the closed state pore via the constricted intracellular gate, as a reference value corresponding to prohibited entry (Fig. 4c, red curve). TPeA first interacts with the lower TM2 helices (Fig. 4c, "lower TM2" inset), leading to a deep well in the free energy profile (−8.2 ± 0.7 kcal/mol), after which it encounters a high barrier (19 ± 1 kcal/mol) to cross the narrow intracellular gate, where it dehydrates (Fig. 4c, Extended Data Fig. 6a). Inside the pore, there is a minimum in the hydrated cavity just below the SF (−3.7 ± 0.5 kcal/mol, Fig. 4c, "Cavity" inset) where TPeA buries its alkyl chains in the hydrophobic residues of the pore. As observed in the structure, TPeA interacts extensively with lipids when inside the cavity (Extended Data Fig.6f–g). The estimated equilibrium constant K_D for binding inside the pore, based on the free energy profile for TPeA (Fig. 4c; see Methods), is 119 ± 5 μM, being at least an order of magnitude higher than the experimental value of 2.1 ± 0.2 μM [21]. This reduced calculated affinity may be due to a K^+ ion observed to slip out of the SF and into the cavity as the filter collapses in the MD simulation when TPeA binds to the pore, which would also be expected to increase the barrier for TPeA to bind in that region (further details in Supplementary Fig. 3).

The high free energy barrier for TpeA to pass through the closed gate suggests low rates of passage. The unimolecular Kramer's rates for binding and dissociation of TPeA based on the 1-dimensional (1D) free energy profile are 0.0066 ± 0.0026 s^{-1} and 0.0040 ± 0.0016 s^{-1}, respectively (Fig. 4c). The estimated bimolecular association rate constant for overcoming the barrier at the bundle crossing and binding to the pore from water (see Methods), k_{on}, is 33 ± 20 $M^{-1}s^{-1}$, which is four orders of magnitude slower than the experimental estimate of 0.14 ± 0.02 $\mu M^{-1}s^{-1}$ [21] (agnostic to the pathway), suggesting TPeA is unlikely to enter the pore via this pathway.

Favored blocker entry via the membrane-facing fenestrations

We next used US to describe membrane partitioning and subsequent crossing of TPeA through one of the four side fenestrations (Fig. 4a). The free energy profile for 1-palmitoyl-2-oleoyl-sn-glycero-3-phosphatidylethanolamine (POPE):palmitoyl-2-oleoyl-sn-glycero-3-phosphatidylglycerol (POPG) (3:1) bilayer partitioning (Extended Data Fig. 5d) shows a strong preference for TPeA to move from water into the membrane, preferring to reside with its center of mass ~16 Å from the bilayer center (Extended Data Fig. 5d, left inset). It then experiences a steep barrier to approach the bilayer center, owing to membrane deformations around the localized charge of the ammonium group (Extended Data Fig. 5d, right inset). The calculated membrane partition coefficient, P = 780 ± 200, strongly favoring the membrane interface over water (~1 TPeA in water for every 780 in the bilayer at equilibrium), explains our observations from unbiased MD simulations (Extended Data Fig. 5a–b).

To determine TPeA entry into the pore through fenestrations from the bilayer interface, we carried out 2D US as a function of both the lateral x and vertical z coordinates spanning the pore, fenestration and membrane interface. The 2D free energy map reveals the lowest free energy path for TPeA to enter the pore via the fenestration (Fig. 4b, dashed line; Supplementary Movie), which passes through the bottom of the fenestration aided

by interactions with E92 (Fig. 4a, c, "fenestration" inset, near $z = -4$ Å, Extended Data Fig. 6d), leading to a barrier of ~6 kcal/mol. This value is ~13 kcal/mol lower than that encountered when the blocker attempts to access the pore via the intracellular gate.

Inside the pore, TPeA binds preferentially just below the SF (z=5.5 Å), a similar position as in the cryo-EM map (z=7.4 Å; compare Fig. 4c "pore" inset to Fig. 2b, f, i), with lipid tails again contributing to its solvation (Extended Data Fig. 6d–g). The free energy at the upper pore binding site is similar to that at the membrane interface (similar blues in Fig. 4b), considerably more negative than in bulk water (Extended Data Fig. 5c). To compare with the energy profile via the intracellular gate (Fig. 4c, red line), we also derived a 1D free-energy profile for TPeA entry via the fenestrations from the 2D US (Fig. 4c, blue line). TPeA encounters a free energy minimum (−2.0 ± 0.1 kcal/mol) upon interaction with E92 and hydrophobic residues on TM2 (Fig. 4c, "fenestration" inset), after which it crosses a barrier of just 4.9 ± 0.1 kcal/mol as it dehydrates to enter the pore (Fig. 4c, "pore" inset, Extended Data Fig. 6a), with a free energy comparable to that at the membrane interface. Importantly, relative to bulk water, the free energy of TPeA binding inside the pore is consistently ~−4 kcal/mol, whether it is accessed via the gate or via the membrane and fenestration (Fig. 4c, Extended Data Fig. 5d).

As a result of the much-reduced barrier to pass the fenestration, higher Kramer's rates for binding and dissociation of 1.6 ± 0.1 μs^{-1} and 46 ± 1 μs^{-1}, respectively, are calculated, based on the 1D free-energy projection (Fig. 4c). The bimolecular association rate constant, k_{on}, for crossing the barrier at the fenestration and entering the pore from the membrane interface is 19 ± 1 $\mu M^{-1}s^{-1}$, 2 orders of magnitude faster than the experimental value[21] of 0.14 ± 0.02 $\mu M^{-1}s^{-1}$ (see Methods for details and discussion on the approximate nature of a rate based on a Kramer's model using a 1D free energy projection). The fenestration pathway thus appears to be easily capable of supporting the TPeA binding measured experimentally for the closed channel. These calculations indicate that TPeA enters the closed pore from the intracellular side with a strong preference for the membrane-bound fenestration pathway.

Screen for MthK mutants with obstructed fenestrations

To experimentally test this pathway, we introduced mutations in the fenestration designed to obstruct blocker access to the closed pore. From the six residues lining the fenestration, two (I84, F87, Fig. 2b, i) we did not alter since they contribute to the blocker binding site. Furthermore, *in silico* (COOT[38]) mutations of only three (A90, A88 and V91, Fig. 3c) predicted changes in the fenestration size. We changed all three to bulkier side-chain residues, to make the fenestration smaller and more difficult (or impossible) to access the closed pore. The mutants were first screened functionally for altered closed-state TPeA block. We measured TPeA block in both closed and open states using stopped-flow fluorescence assays[21,39]. To determine the TPeA concentration ([TPeA]) where half of the closed channels are blocked ($IC_{50closed}$), channel-reconstituted liposomes were incubated in 0 Ca^{2+} with different [TPeA], and then the channels were rapidly opened with Ca^{2+} to measure the percentage already blocked. For TPeA IC_{50} in the open state (IC_{50open}) the channels were pre-incubated with Ca^{2+}. To determine the kinetics of equilibration of TPeA with closed and open channels, similar experiments were performed by incubating

the channels for different durations, either with or without Ca^{2+}, respectively, with TPeA concentrations determined from IC_{50} experiments.

A88 mutants displayed very low flux (A88F MthK flux rates in Extended Data Fig. 7a), making it impossible to accurately measure block. A88F MthK was predicted to have completely occluded fenestrations *in silico* but its cryo-EM structure (Extended Data Fig. 7e–i, and Extended Data Fig. 8) revealed that the fenestration was remodeled by the rearrangements of F87 and F88, which actually made the fenestration marginally larger and positioned closer to the extracellular side (Extended Data Fig. 7e–g). Although the F88 side chains line the fenestration, those of F87 reoriented to face the pore axis, leading to a narrower permeation pathway (Extended Data Fig. 7h–i) and potentially explaining the lower flux[40 41–43]. Although the A88F mutant was not useful for testing the fenestration pathway due to its low signal to noise ratio and the different-from-predicted fenestration size, it offered a cautionary tale about the dangers of interpreting mutation effects without an experimental structure.

Although the V91F MthK also displayed lower flux than WT, we could measure closed and open TPeA block. However, the [TPeA] required to block V91F (IC_{50}) and the block kinetics in both open and closed states were identical to WT (Extended Data Fig. 7b–d), which suggested that V91F, similar to A88F above, behaved differently than expected, and fenestration access was unaltered. MD simulations of modeled V91F MthK in lipid bilayers indicated that the bulky side chains of F91 indeed point toward the pore axis, rather than the fenestration (Extended Data Fig. 9). This can affect ion permeation, as for A88F above. We also observed that V91F displays an increase in lipid tails penetrating into the pore (from 1.3 ± 0.1 in WT, to 3.9 ± 0.1, Extended Data Fig. 9d), apparently stabilized by the aromatic side chains. A time series of fenestration sizes (determined using HOLE), indicated comparable dimensions for V91F and WT, in agreement with the result from functional assays (Extended Data Fig. 9c).

Impeded TPeA access through A90L MthK narrower fenestrations

Only A90L MthK had a block phenotype different from WT (Fig. 5). Closed block assays for a range of [TPeA] (Fig. 5a) revealed that the same concentrations that blocked WT no longer blocked A90L MthK ($IC_{50closed}$ ~17 μM for A90L, 8-fold larger than WT MthK, Fig. 5b left, compare solid lines for A90L with dashed lines for WT). On the other hand, open A90L is blocked by similar [TPeA] as WT MthK (IC_{50open} ~10 μM for A90L, only 2-fold larger than WT MthK, Fig. 5b right). Importantly, it takes less TPeA to block open than closed A90L channels, opposite from WT (Fig. 5b), with consequences for interpretation of “closed block” data: any [TPeA] that blocks closed would also block open channels, only better. This means that during a closed block experiment, the [TPeA] pre-incubating with closed A90L MthK will also block the channels as they are opened to measure the percentage blocked, and thus the measured blocked fraction will also include open channels[21]. In support of this, TPeA appears to equilibrate with closed A90L channels as fast as with open channels (Fig. 5c), indicating that at the concentrations used, TPeA blocks A90L immediately upon opening and the data are rather a measure of open block. This is in

contrast to WT, where the [TPeA] required to block the open is higher than that for closed channels, and true closed-state block could be measured[21].

Two main scenarios can explain the challenges in measuring closed state block in A90L MthK. In the first, the fenestrations of A90L become too narrow for TPeA entry into the closed pore on the time scale of the assay. In this case, even if there is no closed-state TPeA access, as [TPeA] is increased to measure a closed-state block dose response (Fig. 5b left), open channel block will eventually be measured when the [TPeA] reaches the relevant range (Fig. 5b, right). In the second scenario, the intracellular gate of closed A90L MthK, instead of being sterically shut as in WT, is wide open with the TM2 helices splayed apart akin to the open conformation. In this case, intracellularly-applied TPeA would have equal access to its binding site in both closed and open A90L MthK, leading to the observed similar open and closed state block (Fig. 5 b–c).

To distinguish between these, we solved the single-particle cryo-EM structure of lipid nanodisc-reconstituted closed A90L MthK in the absence of Ca^{2+}. The 3.49 Å resolution structure (Extended Data Fig. 3 and Extended Data Fig. 10) was similar to WT MthK, including a sterically shut intracellular gate (Extended Data Fig. 7h–i), eliminating the second scenario. The only differences between A90L and WT are at the fenestrations (Fig. 5d–f, Extended Data Fig. 7g). L90 points towards the TM2 of neighboring subunit, considerably narrowing the fenestrations in A90L compared to WT, as also indicated by MD simulations (Extended Data Fig. 9c). The smallest fenestration dimension in A90L is ~3 Å (Fig. 5f), which is too narrow to allow facile entry of TPeA (average size ~ 7×9 Å)[21].

Consistent with obstructed blocker entry through smaller portals, lipids were no longer observed bound to the closed A90L fenestrations, and MD simulations also revealed reduced lipid presence compared to WT (0.98 ± 0.05 lipids for A90L compared to 1.3 ± 0.1 for WT; Extended Data Fig. 9d). The bound lipids observed in WT structure were captured presumably because they were stabilized by their tails penetrating through the fenestrations. The smaller fenestrations in A90L MthK are less favorable for lipid tail entry with the lipid binding to the fenestrations weakened, as suggested by MD. Together, the functional and structural data, and the MD strongly argue that the L90 substitution narrowed the fenestrations in A90L MthK so that TPeA is mostly prevented from entering closed channels. This, together with the structural evidence that there is no other pathway by which the closed channel pore can be accessed by blockers, is consistent with a dominant fenestration pathway for TPeA into the closed pore.

Discussion

Here we showed that QA blockers access closed MthK channels via a non-canonical, state-dependent, membrane-facing fenestration path, rather than via the ion conduction pathway through the intracellular entryway, as in open channels. We provided structures of closed MthK in complex with two different blockers, suggesting that the blockers can access and bind in the closed pore. MD simulations calculated a considerably lower free energy barrier for the blocker to access the closed pore through the fenestration than via the ion conduction pathway, consistent with the experimental rates of blocker access[21]. Finally, we validated

this pathway experimentally by showing that mutant channels with narrower/obstructed fenestrations displayed impeded blocker access in the closed state.

These findings shed light on previous data where blockers binding to closed MthK was taken to mean that the intracellular pore entryway remained wide enough in the closed state, implying that the channel gate was at the selectivity filter[21]. This was based on the assumption that the only way into the pore was via the canonical ion conduction pathway. Structures of closed MthK[12] were instrumental in debunking this assumption as they not only showed that the intracellular entryway is too narrow for ions and blockers to access the pore (Fig.1a), but also indicated an alternative access path for blockers, i.e. the membrane-facing fenestrations. Our structures, MD simulations, and functional assays of fenestration mutants showed that TPeA and bbTBA are indeed bound in the cavity of the closed MthK and they access this site via the fenestrations, a non-canonical pathway.

Suggestions that BK channels gate at the selectivity filter[10,11,21] were based on evidence that intracellularly-applied QA blockers can access both open and closed states, as had been found for MthK[21]. This is in contrast with data for voltage-gated potassium channels[44,45] where strict state-dependent intracellular blocker and other probes' accessibility indicated that at least one of the gates restricting permeation was at the intracellular entryway (Fig.1a). Furthermore, blockers access both open MthK and BK channels with similarly high, near diffusion-limited rates[11,21], while they access other open K^+ channels with lower rates[22,46], highlighting similarities between MthK and BK and differences from their K^+ channel relatives. Our finding that QA blockers access closed MthK via membrane-facing fenestrations rather than via the ion-conduction pathway opens up the possibility that this happens in the closely-related BK channels.

Although the existing BK channel structures can accommodate QA blocker entry via the ion conduction pathway in both Ca^{2+}-free and Ca^{2+}-bound conditions (Fig. 1b), it is unclear whether the Ca^{2+}-free structure is a closed state[8], and whether other closed states, with narrower or tightly-shut intracellular gates, are still to be identified[9] (alternatively, the wide intracellular gate in Ca^{2+}-free BK could indicate hydrophobic, or vapor-lock gating where a steric obstruction of the permeation pathway is not required for a closed state[47]). Despite the wide gate, the pore-lining helices in the Ca^{2+}-free are straighter than in the Ca^{2+}-bound BK structure, creating fenestrations similar to those in closed MthK, with conserved residues lining it (Fig. 1b, Extended Data Fig. 4). QA blockers may access the BK pore via these fenestrations as well as via the ion conduction pathway, even if the intracellular gate is wide (molecules with large membrane partition coefficients may prefer a membrane path). This would re-ignite discussions about the gate locations in BK channels. In this context, it is interesting that both BK and MthK, reported to be accessed by QA blockers in the closed state and hence proposed to gate at the SF, possess fenestrations in closed states, while channels where blockers may not access the closed state (KcsA, inward-rectifiers) and believed to gate at the intracellular gate, do not display fenestrations (Fig. 3 and Extended Data Fig. 4).

Lipids were observed bound to the MthK fenestrations and inspection of the density (EMD-21036) of the Ca^{2+}-free BK channel structures[5,7] also indicated unassigned lipid

densities at the BK fenestrations (Extended Data Fig. 4a, e). The state-dependent binding of lipids suggests lipid-dependent gating in these channels, which was previously reported for BK, although the mechanism is still unclear[48 49 50 51]. MthK has not been reported to display lipid-dependent gating, but mutations of a residue lining the fenestration, A88, which would lead to changes in the size of the fenestration and affect lipid binding, were reported to have changes in activity, consistent with a role for lipids in stabilizing closed MthK via binding at fenestrations[40].

Structures of blocker-bound KcsA channels (and open MthK[20]) share features with the structures of blocker-bound closed MthK (Extended Data Fig. 4)[31,32,34,52]. For long-tailed blockers, a conserved phenylalanine right below the SF (F103 for KcsA and F87 for MthK) assumes a different rotamer when blockers are bound (Fig. 2). The down F rotamer in the presence of blocker was associated with a “collapsed”, C-type inactivated selectivity filter[35], and KcsA bound with long-tailed blockers displays a collapsed SF with only two ions in the pore[34], similar to our TPeA- and bbTBA-bound MthK structures (Fig. 2). Filter emptying is also an indication of a non-conductive filter, and simulations have shown that the MthK SF will collapse with only one ion in S4[53]. The ion loss from the MthK SF following blocker binding is also consistent with observations of accelerated C-type inactivation in QA blocker-bound *Shaker* K^+ channels, caused by loss of ions from the pore[29]. The resolution of the selectivity filter in our structures is however not sufficient to differentiate between a collapsed and a conductive filter, although MD simulations showed it collapsed upon TPeA binding.

Fenestrations are increasingly found in structures of many membrane proteins suggesting an emerging general mechanism to regulate transport and entry of hydrophobic molecules inside permeation pathways, bypassing the canonical pore/transporter pathways. Lateral fenestrations were proposed as access points for local anesthetics and antiarrhythmics into the resting state pores of Na^+ channels[54–56]. Calcium channels also display fenestrations, potential entry pathways for dihydropyridines, benzothiazepines and phenylalkylamines[57,58], and fenestrations in TREK-2 channel are used by fluoxetine to enter the pore[59]. In addition, transporters for hydrophobic compounds such as Vitamin A, also have lateral windows that may shuttle these compounds through the membrane[60]. Currently, the physiological role of fenestrations in K^+ channels is unknown[61]. However, the high conservation between the fenestrations in MthK and those in BK, together with their unique state-dependence suggests an evolutionary pressure for preserving these features in calcium-activated potassium channels and an opportunity to identify novel therapeutics.

We reexamined a previous assumption that intracellular blockers access channel pores exclusively via the canonical ion conduction pathway, following our observation that a closed MthK channel structure with a sterically shut intracellular gate, prohibitive to QA blocker entry, is nevertheless blocked by these molecules. We can now reconcile previous functional experiments with structural data by showing how QA blockers can enter and block the closed MthK pore via a non-canonical membrane-facing fenestration path, despite a closed intracellular gate. This investigation illustrates the power of cryo-EM structures, together with atomistic MD simulations, in eliminating scenarios from the list of possible mechanisms inferred from functional studies, especially when structures are

assigned to functional states. In addition, a novel access pathway into the pore of calcium-gated potassium channels opens possibilities to design much needed state-dependent drugs targeting these therapeutically-relevant ion channels.

Methods

Sample Preparation

The MthK WT and A90L mutant channel expression, purification and reconstitution into nanodiscs has been done as described previously[12]. Briefly, XL1-Blue cells transformed with pQE82-MthK was grown at 37°C in Luria-Bertani media until OD600=1, then incubated with 400 μM IPTG for 3 h at 37°C. The cells were sonicated and membranes were extracted using 50 mM decyl maltoside for 2 hours at room temperature. The proteins were purified by the histidine tag binding to a cobalt column, then the histidine tag was cleaved by thrombin. MthK was further purified on a Superdex-200 (GE Healthcare) gel filtration and concentrated by 50,000 MWCO Amicon concentrators (Millipore). MthK was reconstituted into nanodisc with 3:1 POPE:POPG for the blocker-free, A90L mutant, and TPeA dataset, and 3:1 DOPC:POPG for the bbTBA dataset.

Grid preparation and EM data collection

The blocker-free MthK sample had cadmium chloride (Sigma-Aldrich) added to a concentration of 1mM, which was immediately used to freeze cryo-EM grids. Cadmium (Cd^{2+}) was meant to be an activator in this sample as it was previously reported to activate MthK[62]. Although we used ~20 folder higher concentration than the reported EC50 for Cd^{2+} activation, most of the particles are in the closed state with Cd^{2+} density observed in the RCK domains in the high affinity calcium-binding site (C1) but not in the low affinity sites (C2,C3)[12]. This structure is identical to the closed state we previously observed and reported in the presence of Ca^{2+} [12]. We did not follow up on the reason for the lack of activation, although one possibility is that some of the Cd^{2+} precipitated and the final concentration was lower and thus not sufficient for supporting the open state. Here we are only interested in the serendipitously-obtained higher resolution MthK closed state structure with better resolved lipids and selectivity filter than the previously reported structure[12], without further investigation of the mechanism for Cd^{2+} activation.

For MthK with TPeA, EDTA was first added to a concentration of 0.5 mM, then tetrapentylammonium (TPeA) hydroxide solution (Sigma-Aldrich) was added to a concentration of ~1mM. The mixture was incubated for 2 hours at room temperature before freezing the cryo-EM grids. For MthK with bbTBA, EDTA was first added to a concentration of 0.5 mM, then *N*-(4-[benzoyl]benzyl)-*N,N,N*-tributylammonium (bbTBA, Spectra Group Limited Inc.) was added to a concentration of 5 mM. The mixture was incubated for 24 hours at room temperature before freezing. The freezing procedure is the same as described previously[12]. Briefly, all samples (~10mg/ml) were supplemented with 3mM Fos-choline-8, Fluorinated (Fos8-F, Anatrace) right before freezing, the grid was plunge frozen in liquid ethane using a Vitrobot Mark IV (FEI, Thermo Fischer Scientific) with blot force 1, blot time 2s. The MthK A90L (~10mg/ml) sample was incubated with 5mM EDTA for 5mins at room temperature and then supplemented with Fos8-F right before

freezing, the grid was plunge frozen in liquid ethane using the Vitrobot Mark IV (FEI, Thermo Fischer Scientific) with blot force 1, blot time 2s.

The blocker-free and TPeA-bound MthK datasets were collected on a Titan Krios (FEI, Thermo Fischer Scientific) equipped with a Cs corrector and imaging filter operated at 300KV. Images were collected on a K2 direct electron detector (Gatan) in counting mode using Leginon[63]. For the blocker-free MthK dataset, the pixel size is 1.096 Å/pixel and total dose is 51.53 e/Å2. For the TPeA-bound MthK dataset, the pixel size is 1.1 Å/pixel and total dose is 52.23 e/Å2. The bbTBA-bound MthK dataset was collected on an Arctica Talos (FEI, Thermo Fischer Scientific) operated at 200KV. Images were collected with a K3 direct electron detector (Gatan) in super resolution mode using Leginon[63]. The pixel size is 1.096 Å/pixel and total dose is 52.52 e/Å2. The blocker-free MthK A90L closed dataset was collected on Titan - Krios G3i (FEI, Thermo Fischer Scientific) equipped with a Cs corrector and imaging filter operated at 300 KV. Images were collected on a K3 direct electron detector (Gatan) in super resolution mode using Leginon[63]. The pixel size is 0.5413 Å/pixel and total dose is 65.19 $e^{-}/Å^{2}$.

Cryo-EM data processing and Model building

All datasets were processed in Relion3.0[64]. The frames were aligned and dose weighted with Relion Motioncor2[65]. The contrast transfer functions (CTF) were estimated with CFTFIND4[66]. Particles were auto picked, extracted, and used for 2 rounds of 2D classification in Relion3.0. The good classes were selected and used for 3D classification. The closed state particles were selected and used for refinement without imposing symmetry. Focused classification was used to find the particles with best transmembrane domain (TMD), by using a mask surrounding the TMD region and running 3D classification without alignment. The best class was selected and further refined with or without fourfold symmetry. The overall structures of these datasets are nearly identical to the MthK closed structure we reported before[12]. The MthK closed structure (PDB 6U6D) was docked into the cryo-EM maps first with UCSF Chimera[67]. Then, the cryo-EM maps were carefully checked for extra density, and Cd^{2+}, TPeA, bbTBA, and lipids were manually built in Coot[68]. The structures were further refined by PHENIX real space refinement[69] for several rounds. The MthK-A90L and the TPeA-bound MthK-A88F datasets were processed similarly in Relion3.0[64].

Stopped-flow Tl^{+} flux assay

Stopped-flow experiments were performed using a sequential-mixing stopped-flow spectrofluorimeter (Applied Photophysics, Leatherhead, UK). A90L MthK protein was first reconstituted into large unilamellar vesicles (LUVs) containing the fluorophore ANTS (8-Aminonaphthalene-1,3,6-trisulfonic acid, Life Technologies), as described[21,39]. LUVs were made of POPE:POPG (3:1) and contained 450 μg channel for 15 mg lipid mixture.

For measuring closed state block, LUVs containing A90L MthK (in 140 mM KNO_3, 10 mM HEPES, pH 7.0) in the absence of Ca^{2+} were mixed with 2X [TPeA] (2, 12, 20, 60, and 200 μM TPeA) in premix buffer (140 mM KNO_3, 10 mM HEPES, pH 11.7) for 10 s. Then, the

mixture was immediately mixed with 34.4 mM Ca^{2+} and 1X [TPeA] (1, 6, 10, 30 and 100 μM TPeA) in quench buffer (50 mM $TlNO_3$, 94 mM KNO_3, 10 mM HEPES, pH 8.5).

For the open state block measurements, LUVs containing A90L MthK were first incubated with 34.4 mM Ca^{2+} and 2X [TPeA] in premix buffer for 100 ms, followed by immediately mixing with 17.2 mM Ca^{2+} and 1X [TPeA] in quench buffer.

For measurement of activity at 0 mM TPeA, LUVs containing A90L MthK were mixed with premix buffer for 100 ms before immediately mixing with 34.4 mM Ca^{2+} in quench buffer.

For both closed and open block experiments, three biological repeats with three separate protein and LUV preparation were performed. In each biological repeat, six measurements were performed per one concentration of TPeA.

MD Simulations of TPeA binding

Basic MD simulations details—MD simulations were performed starting with the closed conformation of the WT, A90L and V91F MthK channel embedded in lipid bilayers containing 1032 lipids (POPE:POPG in ratio 3:1; to match that used in the cryo EM nanodiscs), hydrated by 90,470 explicit TIP3P water molecules and 150 mM KCl solution (containing 623 K^+ and 245 Cl^- ions, to ensure a charge neutral system), totaling 435,510 atoms. In the case of systems simulating TPeA, K^+ ions were replaced with TPeA. The systems were built with CHARMM[70] and equilibrated and simulated with NAMD2.13, NAMD2.14[71] and purpose-built supercomputer Anton 2[72] (only for WT systems). During the equilibration, harmonic restraints (10 kcal/mol/$Å^2$) were applied to all heavy atoms and slowly released over 2 ns, followed by 1 ns of initial equilibration without any restraints. The CHARMM36 lipid[73] and CHARMM22 protein force fields[74] with CMAP corrections[75] were used, assuming standard protonation states for titratable residues. Corrections to non-bonded interactions were applied to the interactions between K^+ ions and backbone carbonyls (depth 0.102 kcal/mol and position 3.64 Å of minimum) to better match experimental free energies of ion solvation in liquid amides, N-methylacetamide[76]. Parameters for TPeA and bbTBA were generated with the CHARMM General Force Field web server ParamChem (interface version 1.0.0 and force filed version 3.0.1)[77]. The NPT ensemble was imposed by using a Langevin piston[78,79] in NAMD (Martyna-Tobias-Klein barostat on Anton 2[80]) to maintain a pressure of 1 atm, and a Nosé-Hoover thermostat[81,82] to maintain a temperature of 303 K. Bonds to hydrogen atoms were maintained with the RATTLE algorithm[83] and electrostatic interactions calculated with Particle Mesh Ewald[84] with a grid spacing of 1.5 Å and 6th order B-spline mesh interpolation in NAMD (Gaussian split Ewald method[85] on Anton 2 with size and spreading optimized by Anton) with a neighbor list distance of 15 Å and a real space cutoff of 12 Å with energy switch distance of 10 Å.

Unbiased TPeA Flooding simulations—Flooding simulations were performed by replacing K^+ with 90 TPeA ions (deleting overlapping water molecules) using the CHARMM[70] program, resulting in an initial TPeA concentration of 50 mM. Rapid partitioning of TPeA ions to the membrane resulted in a low concentration in bulk solution at equilibrium. The system was simulated for 4 μs on purpose-built supercomputer Anton

2^{72}. The free energy surface for TPeA was calculated as $W(r,z) = -k_B T \ln[\rho(r,z)] + C$, where ρ is the unbiased probability distribution as a function of the radius, r, and z position, with constant C chosen to set the zero of the free energy in bulk electrolyte.

Umbrella sampling simulations for gate entry of TPeA—US simulations[86] were performed for TPeA entering MthK though the closed gate. One K^+ ion was replaced by a TPeA ion. Initial windows were created by dragging TPeA using steered MD with a harmonic force constant of 2.57 kcal/mol/Å^2 for 1ns/Å though the gate. The paths were separated into 48 windows at z=−25 to 22 Å, with 1 Å spacing. In each window, the ion was held near the window central position by harmonic constraint with a 2.57 kcal/mol/Å^2 force constant, ensuring overlapping distributions for neighboring windows. To increase sampling efficiency, the radial position of the ion was constrained with a flat-bottom potential to keep it in a cylinder of 10 Å with a force constant 10 kcal/mol/Å^2. Free energy profiles were then calculated using the Weighted Histogram Analysis Method (WHAM)[87]. Mean and error (reported as $\pm 1/2 \bullet \Delta\mathscr{W}(z)$) were calculated by dividing the data into 2 blocks. Simulations were run for 55 ns and 120 ns, totaling ~2.6 μs and ~5.8 μs of simulation. The fist 42 and 98 ns were discarded following convergence to within 1 kcal/mol (Supplementary Fig. 2a–b).

Umbrella sampling simulations for fenestration entry—US simulations were performed for TPeA movement from the membrane interface though the fenestration to the closed MthK pore. For initial 1D US, configurations for each window were created using steered MD with a harmonic force constant of 10 kcal/mol/Å^2 moved in the x direction a rate of 2 ns/Å. The paths were separated into 32 windows at x=0 to 31 Å (relative to the center of mass of the fenestrations; residues 84, 86, 87, 90, 91 and 94 with x being parallel to the vector that passes though opposite fenestrations (Supplementary Fig. 2a; inset), with 1 Å spacing. In each window, the ion was held near the window's central position by harmonic constraint with 2.57 kcal/mol/Å^2 force constant. The transverse position of the ion was constrained with a flat bottom cylindrical potential to keep it in a cylinder of 10 Å with a force constant 10 kcal/mol/Å^2, however this potential was not felt by the ion and did not influence results. Free energy profiles were calculated using WHAM, with mean and standard error calculated by dividing the data into 5 ns blocks. Simulations were run for 80 ns, totaling 2.5 μs, with the first 62 ns discarded following convergence to within 1 kcal/mol (Supplementary Fig. 2c). This 1D US yielded the free energy profile shown in Extended Data Fig. 5c. The profile revealed an attractive well for TPeA binding just outside the fenestration near x=13 Å, as well as inside the pore (x<3 Å), but it can be seen that the approach failed to properly sample the barrier at the fenestration, with a discontinuity near x=10 Å where the TPeA ion passed though the fenestration (Extended Data Fig. 5c).

The 1D US describing lateral entry of TPeA therefore struggled to sample fenestration passage because TPeA remained strongly bound to the protein (at x~13 Å in Extended Data Fig. 5c) instead of moving up into the fenestration. As a result, 2D US was needed to ensure equilibrium sampling TPeA movement though the MthK fenestration. The map was separated into 291 windows with 1 Å spacing from x=0 to 20 Å and z=−7 to +5 Å, plus additional windows inside the pore from x=0 to 5 Å with z up to +8 Å), covering a region that spans the pore, fenestration and membrane interface. Initial windows were chosen from

1-dimenional US for TPeA entering though the fenestration by picking the frame closest to the center of the window. In each window, the ion was held near the central position by harmonic constraint with a 2.57 kcal/mol/Å^2 force constant in each dimension. Each window was simulated for 20 ns, totaling in ~5.8 μs of simulation. Free energy profiles were then calculated using 2D WHAM[88].

We have derived a free energy profile for TPeA fenestration entry in the x direction, $W(x)$, from the 2D free energy map, $\mathscr{W}(x, z)$, via

$$W(x) = -k_B T ln \int e^{-\mathscr{W}(x,z)/k_B T} dz + C,$$

with constant C determined by setting $W(x)$ to zero far from the protein, k_B is Boltzmann's constant, T is temperature and integration is over the full range of z sampled during 2D US. To extend the resultant free energy profile further away from the protein in the membrane interface, the 2D US simulations were supplemented with the 1D US and flooding simulations (which sampled well the movements away from the protein) to create an overall 1D projection along the x-axis in Fig. 4c (blue line). This was done by including the timeseries from 1D sampling as additional windows in the 2D WHAM with zero force constant in the z direction, as well as including each individual molecule in the flooding simulations as separate additional windows with zero force constant in either direction. Convergence of the 2D US was judged by analyzing changes in the 1D projection, $W(x)$, to within 1 kcal/mol, which occurred after 8 ns (Supplementary Fig. 2d). The first 8 ns were therefore discarded before computing the final free energy map in Fig. 4b. Mean and error (reported as $\pm 1/2 \bullet \Delta\mathscr{W}(x)$) were calculated by dividing the data into 2 equal blocks. Although this projection assumes an equilibrium distribution of vertical movements, it serves to approximate the free energy changes associated with passing from the membrane to the pore of the channel, incorporating a range of possible pathways, similar to the optimal pathway (Fig. 4b, dashed curve).

Estimation of rate constants—The rate constants for entering or leaving the pore via the two pathways were estimated using the Kramer's transition rate[89,90]

$$k^* = \frac{D(\xi_{\text{barrier}})}{2\pi k_B T}[-W''(\xi_{\text{barrier}})W''(\xi_{\text{well}})]^{1/2} e^{-\Delta W_{\text{activation}}/k_B T},$$

where $W(\xi)$ is the 1D free energy profile as function of $\xi = z$ or x, for gate or fenestration entry, respectively, $D(\xi_{\text{barrier}})$ is the diffusion constant at the top of the barrier (see below), $W''(\xi)$ is the second derivative/curvature at the barrier or well, and $\Delta W_{\text{activation}}$ the activation barrier. Using a Kramer's rate model based on a 1D free energy projection may not fully incorporate friction in secondary coordinates and may yield elevated estimates of the true rates. Curvatures of extrema were determined by fitting a second degree polynomial to minima and maxima of the free energy profiles in Fig. 4b and Fig. 4c (blue line), spanning minima just outside the channel and within the pore (-15 Å$<z_{well\ entrance}<$ 4 Å, 4 Å$<z_{barrier}<$ 13 Å and 20.5 Å$<z_{well\ pore}<$ 23.5 Å for entry though the gate and 12 Å$<x_{well\ entrance}<$ 16 Å, 6 Å$<x_{barrier}<$ 11.5 Å and 2 Å$<x_{well\ pore}<$ 5 Å for entry though the fenestration). This

resulted in k^*_{fwd} = 0.0066 ± 0.0026 s^{-1} and k^*_{bwd} = 0.0040 ± 0.0016 s^{-1} for entering the pore via the gate and k^*_{fwd} = 1.6 ± 0.1 μs^{-1} and k^*_{bwd} = 46 ± 1 μs^{-1} for entering the pore via the fenestration.

The Kramer's rate constants for movement along the reaction coordinate, ξ, defined as k^* above, are unimolecular rate constants with units of inverse time. We can relate to the bimolecular association rate constants inferred experimentally by combining Kramer's backward rate constant estimates with the relevant equilibrium constants for binding. In the case of the gate entry pathway from water into the pore, we assume that the experimentally measurable bimolecular rate constant, k_{ON}, corresponds to binding inside the pore from bulk aqueous solution, allowing estimation of the association rate constant via

$$k_{on} = K_B(water \rightarrow pore) \times k^*_{bwd} .$$

Using $K_B(water \rightarrow pore)$ = 8.4±3.9mM^{-1} (see calculation below) and k^*_{bwd} = 0.0040 ± 0.0016 s^{-1}, this gives k_{on} = 33 ± 20 $M^{-1}s^{-1}$. Note that if one were to instead describe the rate of crossing from the interfacial free energy minimum into the pore, multiplying k^*_{bwd} by the equilibrium constant $K_B(interface \rightarrow pore)$, the value of k_{on} would be reduced three orders of magnitude, further demonstrating that this pathway is forbidden.

For entry though the fenestration pathway we assume that, due to the rapid partitioning of TPeA into the membrane interface, the bimolecular rate constant can be estimated based on the equilibrium constant for movement from the membrane to the pore, such that

$$k_{on} = k_B(memb \rightarrow pore) \times k^*_{bwd} .$$

Using $K_B(memb \rightarrow pore)$ = 0.42±0.01M^{-1}(see calculation below) and k^*_{bwd} = 46 ± 1 μs^{-1}, this gives k_{on} =19 ± 1 $\mu M^{-1}s^{-1}$.

The free energy profile for membrane partitioning in Extended Data Fig. 5d shows a strong preference for TPeA to move from water to membrane, validating the assumption of rapid equilibrium with membrane positions before fenestration crossing. Furthermore, we assume that the x-coordinate adequately captures the slow movements of the ion through the side fenestration. This is justified because, although slow movements in z were observed in US simulations on the simulation timeframe, the barrier is dominated by lateral movements in x in Fig. 4c (blue line). This estimate is expected to be approximate, however, because it is a Kramer's estimate based on a 1D free energy projection. We also note that the protein's 4-fold symmetry, with 4 parallel fenestration pathways, suggests rates would need to be scaled up to 4-fold. Reported estimates of rate constants remain unscaled, however, as this depends on the level of independence of the four fenestrations.

Equilibrium constant for pore binding via the intracellular gate—The equilibrium binding constant (inverse dissociation constant) to a site in the protein from bulk water can be expressed in terms of the full 3D free energy surface $W(x,y,z)$, as function of ion position (x,y,z), using the relationship

$$K_B\left(water \rightarrow site\right) = \frac{\int d^3r\, \mathscr{H}_{\text{site}}(x,y,z)\, e^{-\mathscr{W}(x,y,z)/k_BT}}{e^{-\mathscr{W}(x',y',z')/k_BT}},$$

where $\mathscr{H}_{\text{site}}(x,y,z)$ is a 3D Heaviside step function that takes on a value of 1 when inside the site and 0 when outside. Equilibrium binding constants for binding to the pore site via the intracellular gate were calculated from 1D free energy profiles for pore entry, $W(z)$. One can show that the relationship is given by[91,92]

$$K_B(\ water \rightarrow pore\ ) = \pi R^2 \int_{z_{\min}}^{z_{\max}} e^{-W(z)/k_BT} dz,$$

where z is the reaction coordinate in the direction parallel to the membrane normal and R is the radius of the cylinder that was used during US simulations (R=10 Å) to limit the lateral sampling of ion position (but does not affect K_B itself, due to the definition of $W(z)$)[91,92]. When combining with the Kramer's rate constant to form a bimolecular on-rate (see above) to compare to experiment, we assume that only molecules bound inside the pore's cavity will be in a position to block the channel upon activation. We thus consider only the z range corresponding to binding inside the pore beyond the barrier ($z_{min} = -13$ Å and $z_{max} = 7$ Å), leading to K_B(water→pore) = 8.4 ± 3.9 mM^{-1}, with an inverse value of K_D(water→pore) = 119 ± 5 μM.

Equilibrium constant for pore binding via fenestrations—We now derive a similar expression for the equilibrium constant for binding from the membrane to the pore via a fenestration. We define the initial (dissociated) state as an x,y-translationally invariant membrane with an equilibrium distribution in z from $L/2$ to $L/2$ spanning the bilayer (L=25 Å), and the final (bound) state as a localized site within the region of the protein. In order to define the equilibrium constant, we first need to express the free energy profile for movement laterally in the x direction, $W(x)$, as a projection from the full 3D free energy surface, $\mathscr{W}(x,y,z)$,

$$e^{-W(x)/k_BT} = C\int_{-\infty}^{\infty}\int_{-\infty}^{\infty} H(y,z) e^{-\mathscr{W}(x,y,z)/k_BT} dydz$$

where a Heaviside step function, $H(y,z)$, limits the range of sampling in the orthogonal y and z directions. Setting $W(x') = 0$ at distant membrane position $x = x'$, and using the knowledge that $\mathscr{W}(x,y,z)$ is independent of y when far from the protein, $\mathscr{W}(x',y,z) = \mathscr{W}(x',y',z)$, the constant C becomes

$$C = \left(\int_{-\infty}^{\infty}\int_{-\infty}^{\infty} H(y,z) e^{-\mathscr{W}(x',y',z)/k_BT} dydz\right)^{-1}$$

such that the 1D free energy profile becomes

$$e^{-W(x)/k_BT} = \frac{\int_{-\infty}^{\infty}\int_{-\infty}^{\infty} H(y,z)e^{-\mathscr{W}(x,y,z)/k_BT}dydz}{\int_{-\infty}^{\infty}\int_{-\infty}^{\infty} H(y,z)e^{-\mathscr{W}(x',y',z)/k_BT}dydz}.$$

Consider now a hypothetical binding process from a point in uniform bulk water at $\mathbf{r}' = (x', y', z')$ to the pore site, via the membrane, then the path-independent membrane-site equilibrium constant is

$$K_B(\ memb{\rightarrow}pore\ ) = K_B(\ water{\rightarrow}pore\ ) \times \frac{1}{P(\ water{\rightarrow}memb\ )}.$$

Given the equilibrium constant for binding to a site from bulk water, $K_B(\ water{\rightarrow}site\ )$, above, we define $\mathscr{H}_{\text{site}}(x,y,z) = h(x) \times H(y,z)$, using a second Heaviside step function, $h(x)$, that defines the range of the pore binding site in x, taking on a value of 1 for $0<x<x_{\max}$ and 0 otherwise, leading to

$$K_B\left(water \rightarrow pore\right) = \frac{\int d^3r\, h\left(x\right)H\left(y,z\right) e^{-\mathscr{W}(x,y,z)/k_BT}}{e^{-\mathscr{W}(x',y',z')/k_BT}},$$

which, with definition of the membrane partition coefficient, $P(\ water{\rightarrow}memb\ )$, in the next section, gives the following expression for membrane to pore binding

$$K_B(\ memb{\rightarrow}pore\ ) = \frac{\int d^3r\, h\left(x\right)H\left(y,z\right) e^{-\mathscr{W}(x,y,z)/k_BT}}{e^{-\mathscr{W}(x',y',z')/k_BT}} \times \frac{L}{\int_{-L/2}^{L/2} dz\, e^{-(\mathscr{W}(x',y',z)-\mathscr{W}(x',y',z'))/k_BT}}.$$

Here we have set the reference point in bulk water far from both the protein and membrane at x', y', z'. i.e. We have defined the membrane partitioning process as along a line far from the protein at x', y' across the bilayer from z=-L/2 to L/2. Simplifying

$$\begin{aligned} K_B(\ memb{\rightarrow}pore\ ) &= \frac{\int_{-\infty}^{\infty}\int_{-\infty}^{\infty}\int_{-\infty}^{\infty} dxdydz\, h(x)H(y,z)\, e^{-(\mathscr{W}(x,y,z)-\mathscr{W}(x',y',z'))/k_BT}}{\frac{1}{L}\int_{-L/2}^{L/2} dz\ \ e^{-(\mathscr{W}(x',y',z)-\mathscr{W}(x',y',z'))/k_BT}} \\ &= \frac{\int_{-\infty}^{\infty}\int_{-\infty}^{\infty}\int_{-\infty}^{\infty} dxdydz\, h(x)H(y,z)\, e^{-(\mathscr{W}(x,y,z)-\mathscr{W}(x',y',z'))/k_BT}}{\frac{2}{LY}\int_{-\infty}^{\infty}\int_{-\infty}^{\infty} dydz\, H(y,z)\, e^{-(\mathscr{W}(x',y',z)-\mathscr{W}(x',y',z'))/k_BT}}. \end{aligned}$$

Here we have used the fact that H imposes a limit on z to sample one leaflet of the bilayer. We note that our US simulations used to form the profile in Fig. 4c (blue line) sampled a range of z that covers a half of the membrane where free energies were low (not the central high free energy). At the same time, H imposes a limit in the sampling of the uniform $W(x', y', z)$ in y' to a range Y.

We can now insert the following, obtained from the definition of the 1D free energy profile above

$$\int_{-\infty}^{\infty}\int_{-\infty}^{\infty} dydz\, H(y,z)e^{-\mathscr{W}(x,y,z)/k_BT} = e^{-W(x)/k_BT}\int_{-\infty}^{\infty}\int_{-\infty}^{\infty} dydz\, H(y,z)e^{-\mathscr{W}(x',y',z)/k_BT}$$

or

$$\int_{-\infty}^{\infty}\int_{-\infty}^{\infty} dydz\, H(y,z)e^{-(\mathscr{W}(\mathrm{x},\mathrm{y},\mathrm{z})-\mathscr{W}(\mathrm{x}',\mathrm{y}',z'))/k_BT} = e^{-W(x)/k_BT}\int_{-\infty}^{\infty}\int_{-\infty}^{\infty} dydz\, H(y,z)e^{-(\mathscr{W}(x',y',z)-\mathscr{W}(\mathrm{x}',\mathrm{y}',z'))/k_BT}$$

to obtain

$$K_B\left(memb \rightarrow pore\right) = \frac{\int_{-\infty}^{\infty} h(x)e^{-W(x)/k_BT} \times \left(\int_{-\infty}^{\infty}\int_{-\infty}^{\infty} dydz\, H(y,z)e^{-(\mathscr{W}(x',y',z)-\mathscr{W}(\mathrm{x}',\mathrm{y}',z'))/k_BT}\right)}{\frac{2}{LY}\left(\int_{-\infty}^{\infty}\int_{-\infty}^{\infty} dydz\, H(y,z)e^{-(\mathscr{W}(x',y',z)-\mathscr{W}(\mathrm{x}',\mathrm{y}',z'))/k_BT}\right)}$$
$$= \frac{LY}{2}\int_{-\infty}^{\infty} h(x)e^{-W(x)/k_BT}dx,$$

which we see is independent of the additional restraint on secondary coordinates, $H(y,z)$. The end result depends on the definition of the membrane thickness L, as well as the extent of y sampled, which we have found is fairly uniformly sampled across a range Y~16 Å. For use in estimating the bimolecular on-rate, we use an equilibrium constant for binding inside the pore only, $K_B(\ memb{\rightarrow}pore\ )$, defined by $0<x<11$ Å. The calculated binding constant based on this membrane-pore equilibrium (binding from the membrane interface to inside the pore in Fig. 4c, blue line; $0<x<11$ Å) is $K_B(memb{\rightarrow}pore)=0.42 \pm 0.01\ \mathrm{M}^{-1}$.

Calculation of the membrane partition coefficient—The membrane partition coefficient was determined by performing 1D US simulations of TPeA moving across a lipid bilayer. The same MD simulation details as above were used but a with smaller system without the MthK channel (104 lipid molecules, 4126 TIP3P water molecules, 34 K^+, 9 Ca^{2+} and 1 TPeA). Initial windows were created using steered MD with a harmonic force constant of 10 kcal/mol/Å^2 moved at a rate of 2 ns/Å through the fenestration. The paths were separated into 71 windows at $z=-35$ to 35 Å, with 1 Å spacing. In each window, the ion was held near the window central position by harmonic constraint with 2.57 kcal/mol/Å^2 force constant. The transverse position of the ion was constrained with a flat bottom potential to keep it in a cylinder of 10 Å with a force constant 10 kcal/mol/Å^2, having no impact on the translationally invariant sampling in the x and y directions. Simulations were run for 30 ns, with the first 9 ns and 17 ns discarded following convergence to within 1 kcal/mol, for $-35 \le z \le -5$ Å and $5 \le z \le 35$ Å respectively (see Supplementary Fig. 2e–f). Free energy profiles were calculated using WHAM, with mean and error (reported as $\pm 1/2 \bullet \Delta\mathscr{W}(z)$) calculated from the free energy profiles of the two leaflets. The innermost 10 Å was discarded because it has high free energy and does not contribute to partitioning, and because the membrane deformations caused by the localized central TPeA charge lead

to asymmetry and were thus excluded. However, for the range plotted ($5 \leq |z| \leq 35$ Å) in Extended Data Fig. 5d the PMF was converged and symmetric to within 1 kcal/mol.

The membrane partition coefficient was then calculated as

$$P\left(water \rightarrow memb\right) = \frac{1}{L}\int_{-L/2}^{L/2} e^{-W(z)/k_BT}dz \approx \frac{1}{L}\left(\int_{-L/2}^{-5} e^{-W(z)/k_BT}dz + \int_{5}^{L/2} e^{-W(z)/k_BT}dz\right)$$

where we have approximated $\int_{-5}^{5} e^{-W(z)/k_BT}dz \sim 0$ in the region of high free energy at the center of the bilayer, and where L is the distance across the membrane encompassing the binding site parallel to the z axis, L=50 Å.

Diffusion coefficient for rate calculations—The above rate calculations require an estimate of the diffusion near the barriers in the free energy profiles, which we obtain as a spatially varying diffusion coefficient D(ξ). The diffusion coefficient, where $\delta\xi$ is the displacement in each umbrella window, was estimated for each window by[93]

$$D(\xi) = \lim_{s \rightarrow 0} \frac{-\widehat{C}_v\left(s;\xi\right)\left\langle \delta\xi^2 \right\rangle_i \left\langle \delta\dot{\xi} \right\rangle_i}{\widehat{C}_v(s;\xi)\left[s\left\langle \delta\xi^2 \right\rangle_i + \left\langle \delta\dot{\xi} \right\rangle_i\right] - \left\langle \delta\xi^2 \right\rangle_i^2 \left\langle \delta\dot{\xi} \right\rangle_i}$$

Where $\widehat{C}_v(s;\xi)$ is the velocity autocorrelation function at ξ and $\widehat{C}_v\left(s;\xi\right)$ its Laplace transformation

$$\widehat{C}_v(s;\xi) = \int_0^\infty e^{-st} C_v\left(t;\xi\right)dt$$

To estimate $s \rightarrow 0$ and determine $D(\xi)$, a straight line was fitted to $15 \leq s \leq 50$ and $1 \leq s \leq 10$, for umbrella sampling though the gate (data written with frequency 0.002 ps) and though the fenestration (data written with a lower frequency 0.1 ps), respectively, and extrapolated to 0.

Solvation analysis—In all the US simulations the ion's coordination number was determined calculating the number of water oxygen atoms and protein oxygen atoms within 4.8 Å of TPeA N, which represent the first hydration shells based on the position of the first minima in the radial distribution functions, Extended Data Fig. 6a–d. Furthermore, the lipid coordination numbers for TPeA were determined by counting the number of lipid carbon atoms within 5.85 Å of TPeA carbon atoms (based on the position of the first minima in the radial distribution function), Extended Data Fig. 6e–h.

Molecular Dynamics Flexible Fitting for bbTBA in the MthK pore—Molecular dynamics flexible fitting (MDFF)[94] was used to refine the cryoEM structures in the presence of a potential energy function based on the cryo-EM density map $\Phi(\boldsymbol{r})$, given by $U_{EM}(\boldsymbol{R}) = \sum \omega_j V_{EM}(\boldsymbol{r}_j)$, where ω is the weight for each atom j at $\boldsymbol{r}_j$, and

$$V_{EM}(\boldsymbol{r}) = \begin{cases} \xi\left(1 - \frac{\phi(\mathrm{r}) - \phi_{\mathrm{thr}}}{\phi_{max} - \phi_{\mathrm{thr}}}\right) if\, \boldsymbol{\Phi}(\boldsymbol{r}) \geq \phi_{\mathrm{thr}} \\ \xi \qquad\qquad\qquad\qquad\qquad if\, \boldsymbol{\Phi}(\boldsymbol{r}) < \phi_{\mathrm{thr}} \end{cases}$$

with threshold, Φ_{thr}, to remove noise and scaling factor ξ. ξ was initially set to 0.3 kcal/mol and simulated for 10 ns after which ξ was progressively increased from to 9.3 kcal/mol over 90 ns totalling in 100 ns long simulation. The cross-correlation coefficient between the cryo-EM map and the simulation frame was calculated for the backbone of the protein and bbTBA and F87. The cross-correlation coefficient for the backbone is increasing as the force constant increases but the cross-correlation coefficient for bbTBA and F87 plateaus after 50 ns when the bbTBA has rotated its central benzyl ring (Supplementary Fig. 1).

Simulations A90L and V91F—Simulations with mutated fenestration residues were run for 100 ns with the first 50 ns removed as equilibration. The number of lipids in the pore cavity was evaluated from the number of different lipid chains with any C atoms inside a 7 Å radius sphere (encompassing the pore region where atoms were seen to enter), cantered 6 Å below the COM of the pore domain. Error bars represent the standard deviation from dividing the trajectory into 10 blocks. The size of the fenestration was determined using HOLE and registering the smallest fenestration radius along the x-y plane for each trajectory frame. Error bars represent the standard deviation from dividing the trajectory into 10 blocks.

Extended Data

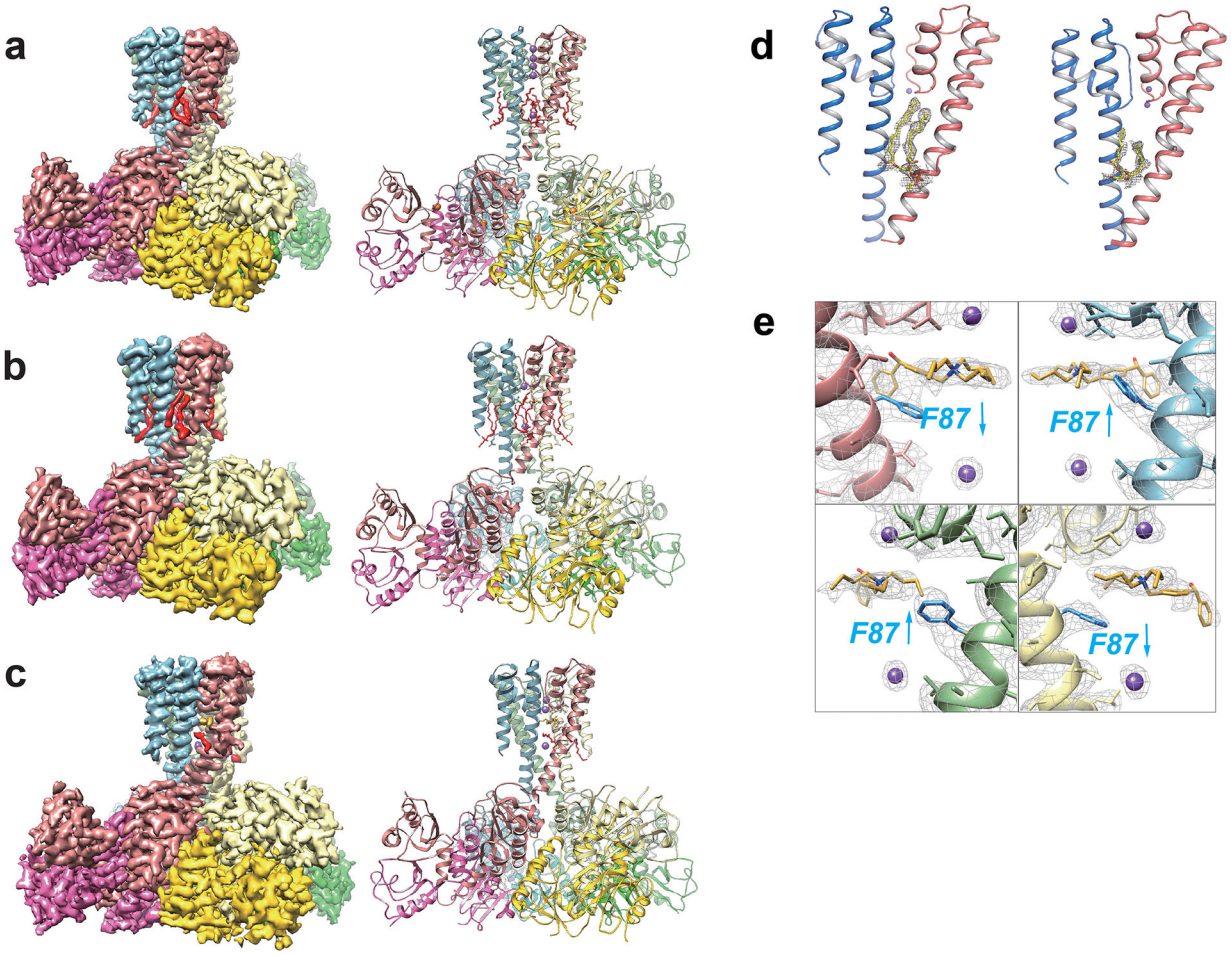

Extended Data Figure 1. Structures of closed MthK with and without blockers.

Cryo-EM map and atomic model of blocker-free (**a**), TpeA-bound (**b**), and bbTBA-bound (**c**) closed MthK viewed parallel to the membrane. Each subunit is in a different color. The lipid bound to the fenestration were colored red. **d**. Lipid density in the structures of MthK with TpeA (left) and bbTBA (right). The lipid is in yellow (for carbon atoms) and red (for oxygen atoms) sticks. The lipid density is an overlayed mesh. The pore region of two adjacent MthK subunits shown as red and blue ribbons cartoon. **e**. Side chains of F87 adopt different conformations in each of the four MthK subunits (red, blue, green, yellow). Density shown as mesh, bbTBA as gold stick and K^+ as purple sphere.

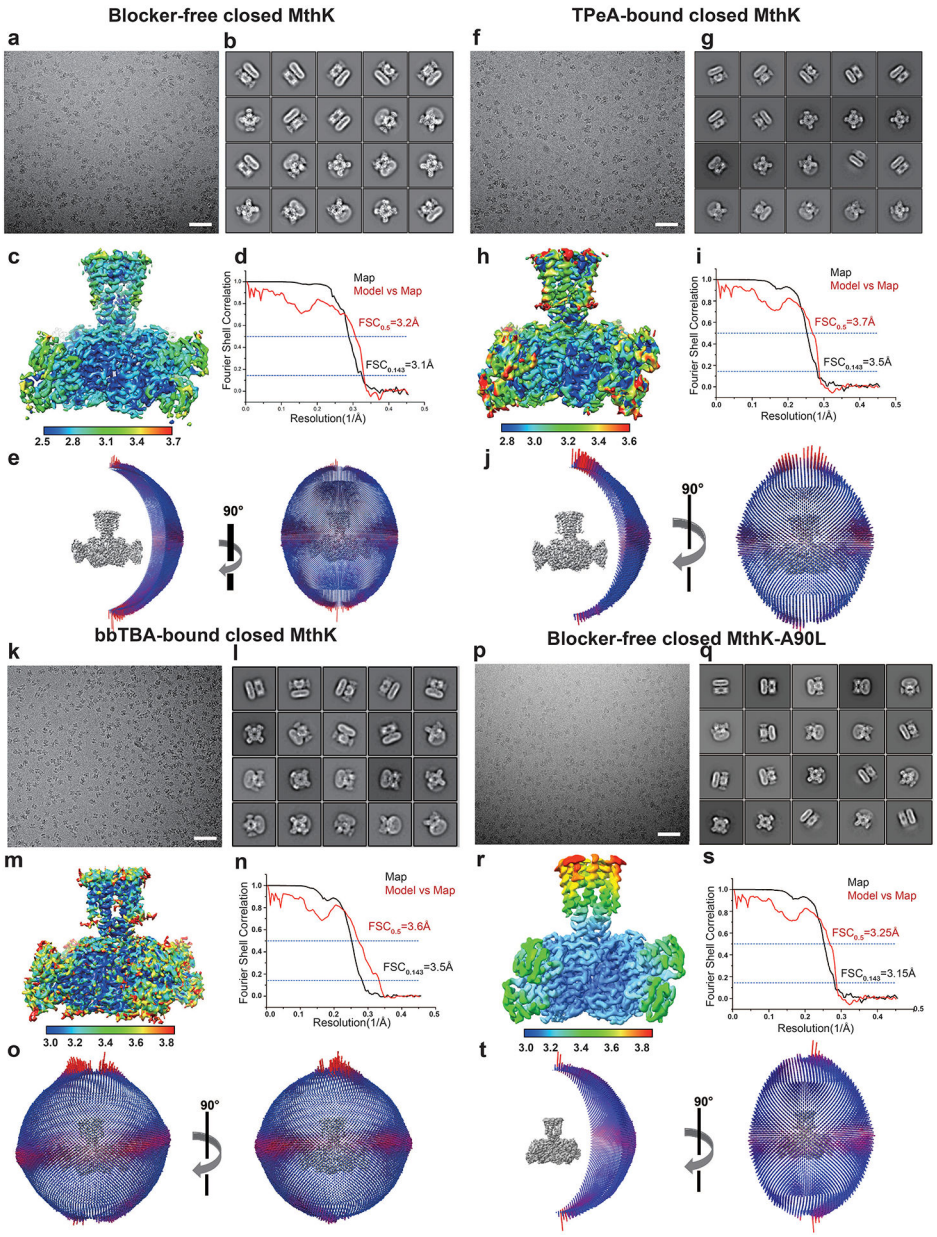

Extended Data Figure 2. Cryo-EM characterization of closed MthK with and without blockers.

Representative micrographs of nanodisc-reconstituted (**a**) blocker-free, (**f**) TPeA-bound, (**k**) bbTBA-bound and **(p)** blocker-free A90L MthK. Calibration bar is 100 nm. **b, g, l, q**. Selected 2D class averages. **c, h, m, r**. Cryo-EM final maps colored by local resolution. **d, i, n, s**. FSC curves for the gold-standard method in black, and for the atomic model with the cryo-EM map in red. **e, j, o, t**. Angular distribution of the particles used for the reconstruction.

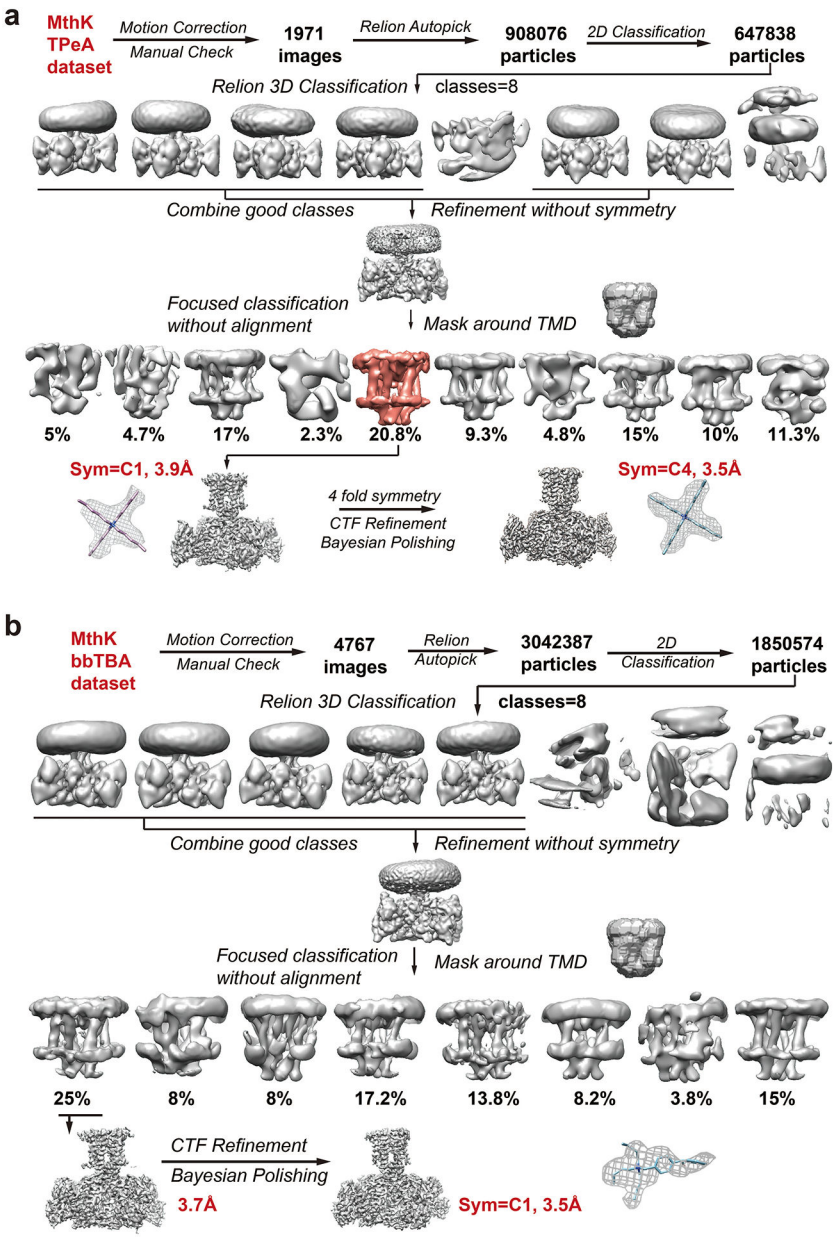

Extended Data Figure 3. Cryo-EM data processing workflows

a. MthK TPeA dataset **b.** MthK-bbTBA dataset. The TPeA (a) and bbTBA (b) densities are shown separately as mesh, with the atomic models as sticks.

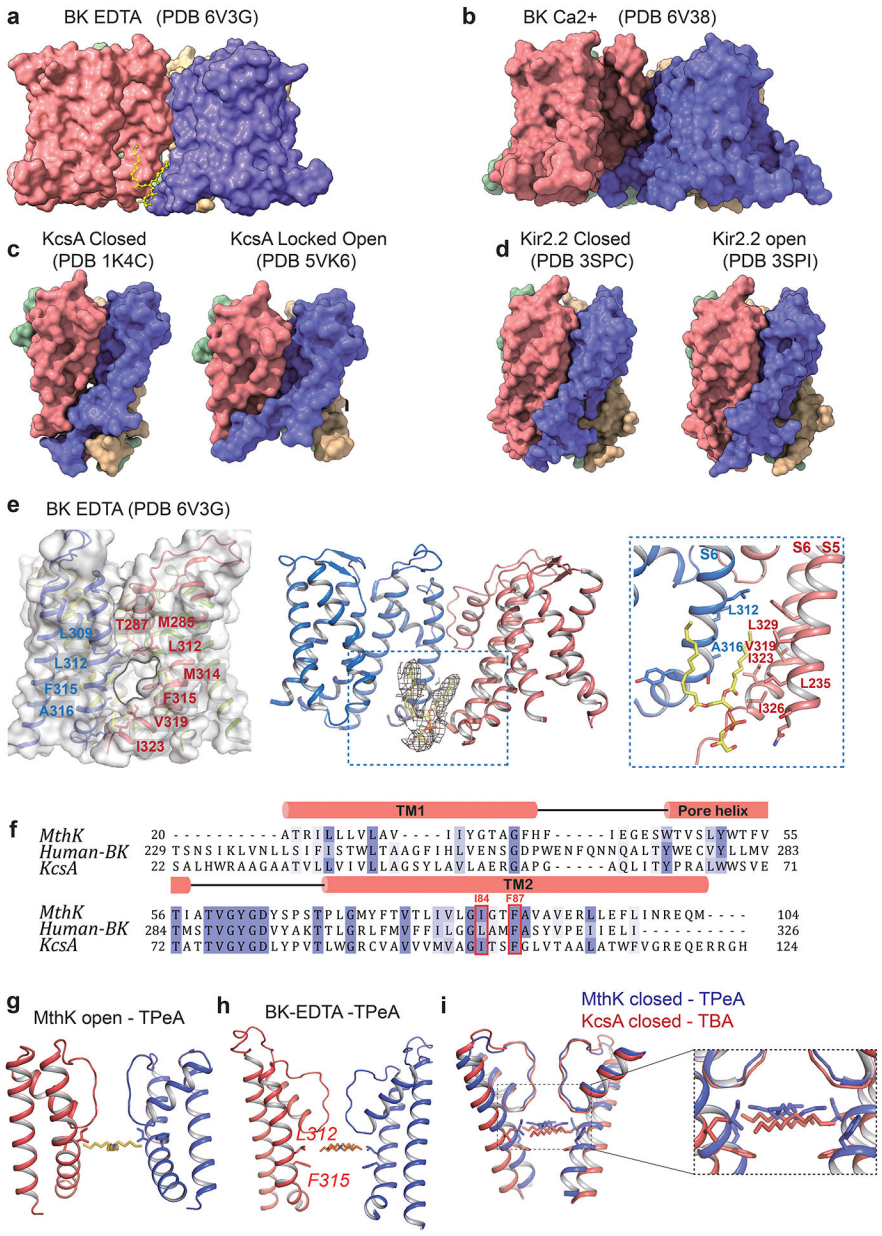

Extended Data Figure 4. Fenestrations and blocker binding sites in other K^+ channels.

a. Fenestrations in human BK channel in EDTA (PDB 6V3G), lipid yellow ball and stick. Part of the fenestration was blocked from view by the VSD. **b**. No fenestration observed in human Ca^{2+}-bound BK channel (PDB 6V38), where fenestration was filled by the bent TM6 helix**. c**. Left: Small fenestration in closed KcsA (PDB 1K4C). Right: No fenestration in locked-open KcsA (PDB 5VK6). **d.** No fenestrations in closed (PDB 3SPC) or open (PDB 3SPI) Kir2.2, respectively. **e**. Left: Size of fenestration (dashed line) in BK with EDTA(PDB 6V3G). Protein rendered in surface representation. The VSDs and part of the S5 helix of the red subunit are removed for clarity. The surrounding residues are labeled sticks. Fenestration is formed by S6 helices from 2 adjacent subunits. Middle: lipid (mesh) binding in BK fenestration. Dashed rectangle indicated the region shown in the right panel,

where surrounding residues are labeled sticks. **f**. Sequence alignment of the pore regions of MthK, Human BK and KcsA channels. Residues interacting with blockers (boxed red) are conserved. Identity and homology are indicated as dark and light purple, respectively. **g**. Modeling of TPeA binding in MthK open state. I84 and F87 side chains are shown as sticks. Note that the side chain of F87 has rotated and no longer contributes to TPeA interaction. **h**. Modeling of TPeA binding in BK channel. The side chains of L312 and F315 are shown as labeled sticks. **i**. Overlay of MthK-TpeA and KcsA-TBA (PDB 2JK5) structures. The pore region of two opposing subunits are shown as red and blue ribbons cartoon. TPeA and TBA are shown as sticks.

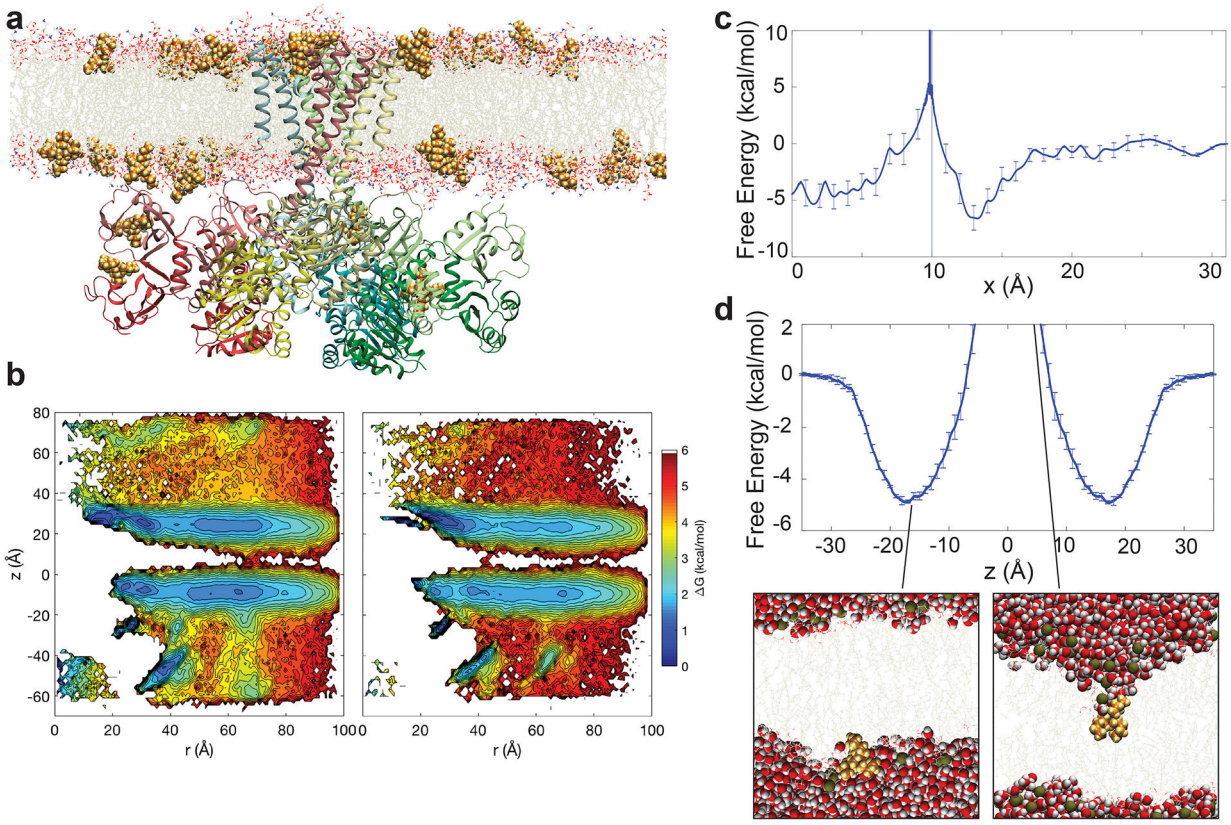

Extended Data Figure 5. MD simulation of TPeA binding and membrane partitioning.

a. Attempted unbiased "flooding" snapshot of MD simulation for $TPeA^+$ entering the closed MthK channel (after 4 μs). **b**. The free energy for TPeA for the first 2 μs (left) and the last 2 μs (right) of the simulation. **c**. TPeA entering MthK though the fenestration (note the different free energy scales in each panel). The free energy profile for the TPeA molecule is flat in the membrane, as TPeA comes closer to the channel there is a gradual slope and a minimum of −7 kcal/mol at x=13 Å. The TPeA molecule then encounters a barrier with the discontinuity at x~10 Å, due to lack of sampling, where the TPeA molecule is trying to enter in between the two TM2 helices, motivating the need for enhanced sampling methods in Fig.4. There is a minimum at x<7 Å where TPeA is inside the MthK pore. **d**. Free energy profile for membrane partitioning using 1D US reveals a free energy minimum of −4.9 ± 0.7 kcal/mol relative to bulk water, extending deep inside the bilayer, reaching to ~12 Å from

the center with only ~1 kcal/mol penalty. Error bars are based on asymmetry of the free energy in left and right leaflets. Insets show TPeA positioning in the membrane at the free energy well (left) and membrane deformation due to interactions between the TPeA ion and water and lipid head groups when TPeA moves closer to the membrane center (right).

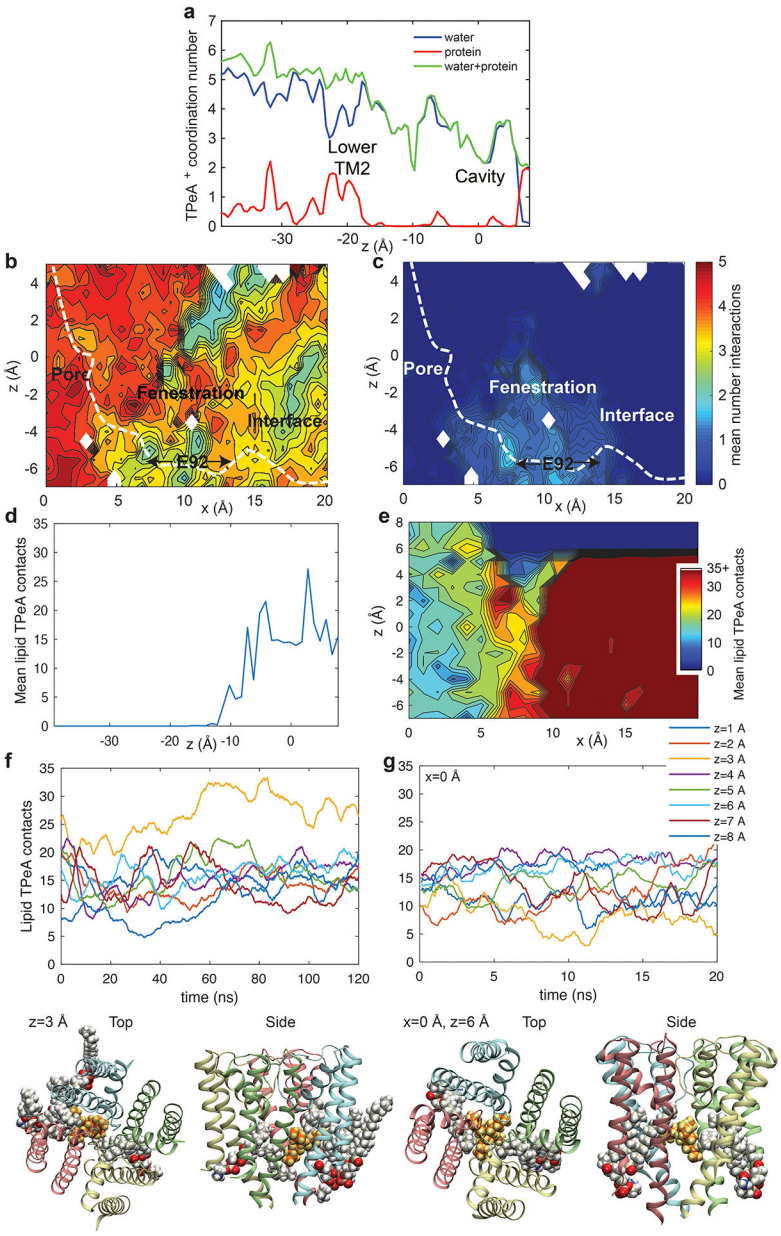

Extended Data Figure 6. Coordination numbers for TPeA+ ions and lipid-TPeA interactions during entry to the pore.

a. Coordination number for TPeA entering though the gate. As the TPeA molecule enters through the gate the nitrogen dehydrates progressively (blue line). It can also be seen to interact with backbone carbonyl oxygens and carboxylate oxygens (red line). **b**. Mean number of interactions between the TPeA N and water molecules. When TPeA crosses though the fenestration it is forced to dehydrate, before rehydrating in the pore. **c**. Mean

number of interactions between the TPeA N and protein oxygen atoms. The crossing of the fenestration is helped by interactions between the TPeA N and the protein. **d-e** describe lipid interactions with TPeA from 1D US simulations for TPeA entering though the gate: **d**. Mean number of lipid C -TPeA C interactions for each window; and **e**. number of lipid C -TPeA C interactions over time for TPeA at 1 Å ≤ z ≤ 8 Å. Insets below show typical lipid-TPeA interactions at z=3 Å. **f-g** describe lipid interactions with TPeA in 2D US simulations for TPeA entering though the fenestration: **f**. Mean number of lipid C -TPeA C interactions; and **g**. number of lipid C -TPeA C interactions over time for windows with TPeA at x= 0 Å and 1 Å ≤ z ≤ 8 Å. Insets below show lipid-TPeA interactions at x= 0 Å and z=6 Å.

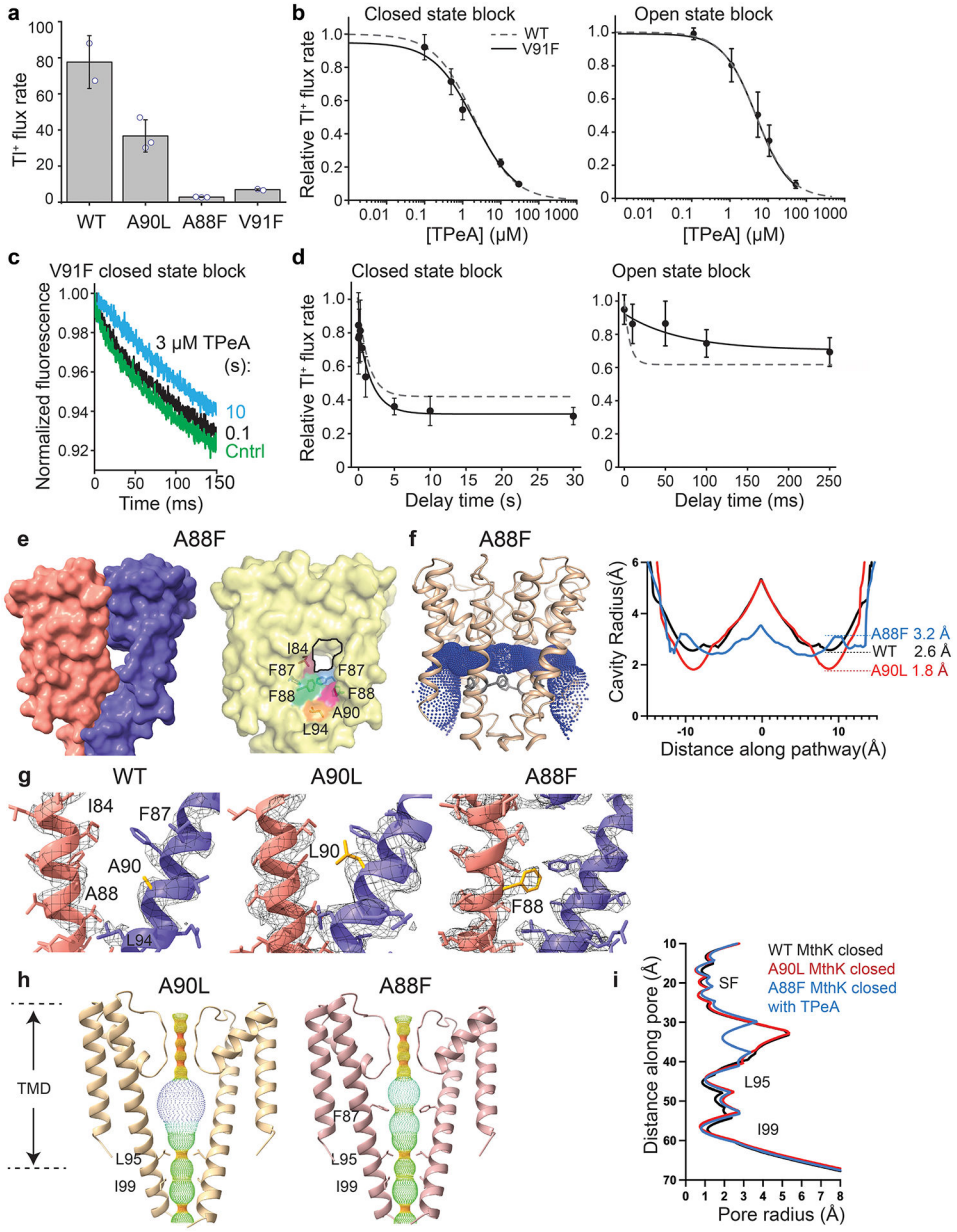

Extended Data Figure 7. TPeA block and structures of MthK fenestration mutants.

a. Tl^+ flux rates of wild-type, A90L, A88F and V91F MthK after activation by 17.2 mM Ca^{2+} for 100 ms. Data are mean ± S.D. of 2–3 biological repeats. **b.** TPeA block dose-response curves of closed (left) and open (right) V91F MthK after 10 s and 100 ms incubation, respectively ($IC_{50closed}$ = 2.05 ± 0.5 μM, IC_{50open} = 4.55 ± 0.1 μM). For comparison, the graphs for MthK WT in dotted lines after the same incubation time are overlayed, from Posson et al. (2015)[21]. Symbols are mean ± S.D of n=3 biological repeats**.** **c**. Fluorescence quench traces after incubating MthK V91F (in 0 Ca^{2+}) with 3 μM TPeA for 0.1 (black) and 10 (cyan) s and no blocker control (green) (lines include 6 repeats each, see Methods). **d**. TPeA equilibration plots for closed (left) and open (right) V91F MthK with 3 μM TPeA from data as in **c**. Solid lines are fits with a first-order exponential decay function, with τ_{closed}= 1.86 ± 0.40 s, and τ_{open}= 83 ± 0.66 ms. The dashed lines are the equilibration plots for 3 μM TPeA with WT MthK, from Posson et al. (2015))[21]. Symbols are mean ± S.D of n=3 biological repeats**. e**. Cryo-EM structure of A88F MthK closed state displays lateral fenestrations between two TM2 helices from adjacent subunits, rendered as in Fig. 3a to be compared with WT (left) and to highlight fenestration size and the residues that line it (right). The introduced F88 faces towards the TM2 of neighboring subunit and F87 changes orientation so that the fenestration is now closer towards the extracellular side and similar in size to WT. **f**. Fenestration calculated using the program HOLE indicates a ~3.2 A radius for A88F. Plots of the fenestration cavity radius for WT, A90L, and A88F, as indicated. **g**. Density (grey mesh) detail of the fenestration area for WT, A90L, and A88F with 2 adjacent subunits (shown in cartoons of different colors). Side chains are indicated and those of L90 and F88 are in yellow sticks for emphasis. **h**. HOLE plots for the pores of A90L (left) and A88F (right). Only two opposing subunits shown. **i**. Pore radii as a function of the distance along the pore calculated from **h**. Selectivity filter (SF), L95, and I99 indicated.

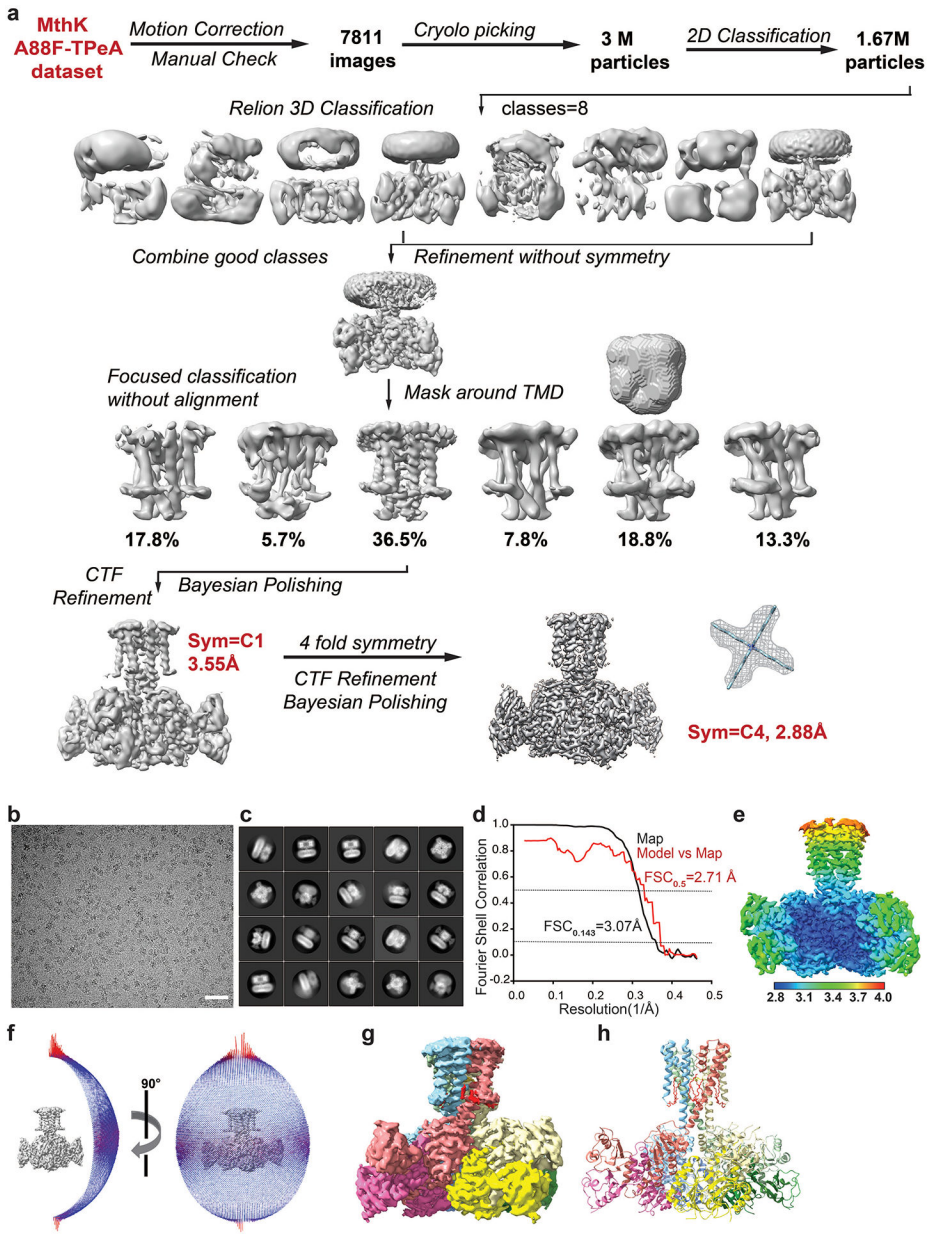

Extended Data Figure 8. Cryo-EM data processing workflow and characterization of MthK-A88F TPeA-bound closed state.

a. Processing workflow for A88F-TPeA dataset, TPeA densities in the maps with C4 symmetry (mesh), TPeA molecule (stick). **b**. Representative micrographs of nanodisc-reconstituted TPeA-bound A88F-MthK. Calibration bar, 100 nm. **c**. Selected 2D class averages. **d**. FSC curves for the gold-standard method in black, and for the atomic model with the cryo-EM map in red. **e** Cryo-EM final map colored by local resolution. **f**. Angular distribution of the particles used for the reconstruction. **g**. Cryo-EM map, and **h**. Atomic model of TPeA-bound A88F-MthK showing the lipid bound in fenestration in red.

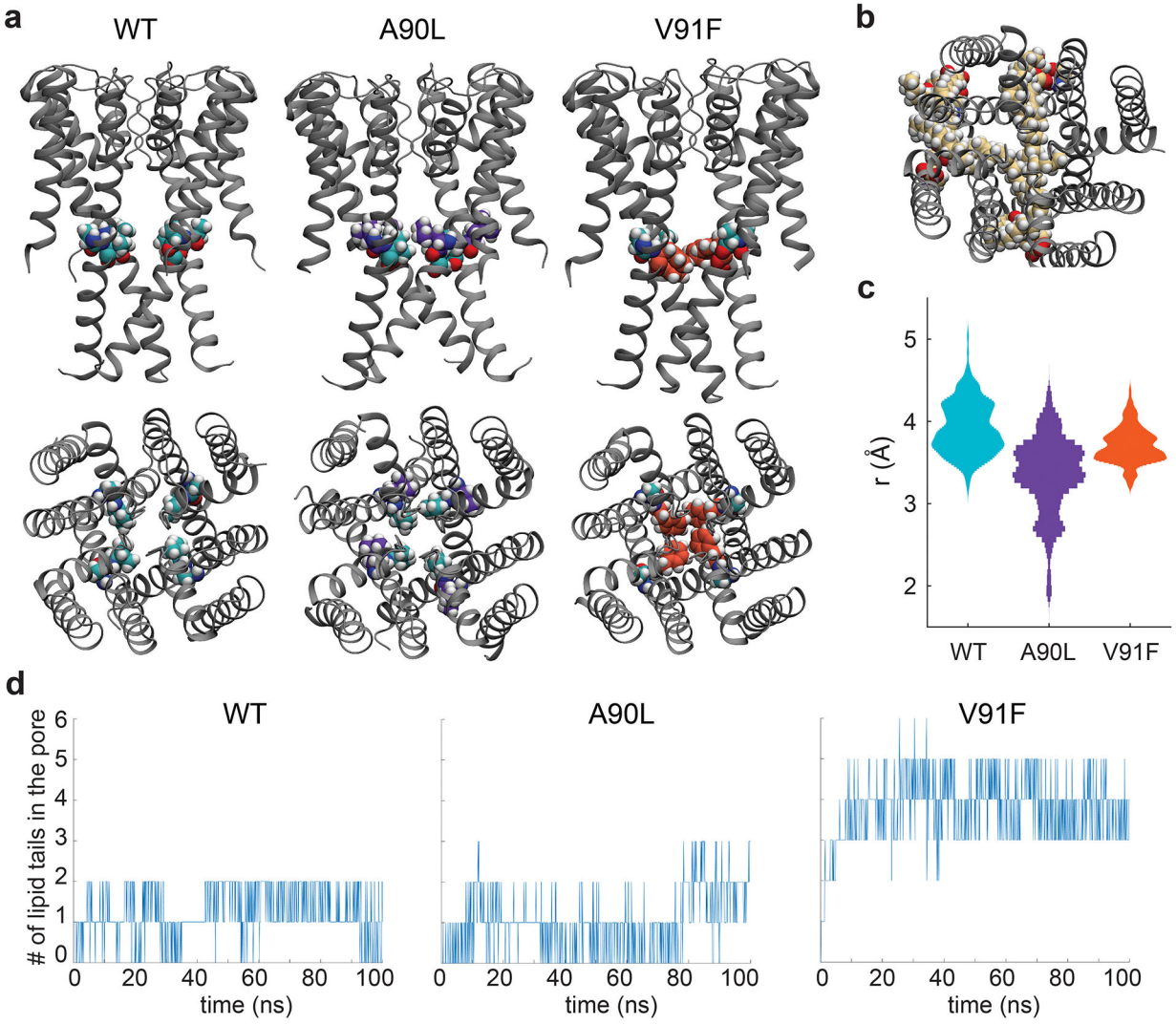

Extended Data Figure 9. MD simulations of MthK WT, A90L and V91F.

a. Representative structures from MD simulations of WT MthK (left), A90L-MthK (middle) and V91F-MthK (right) with side (top row) and top (bottom row) view. The sidechains of residues 90 and 91 are shown as colored spheres in cyan for unmutated residues, purple for L90 and red for F91. **b**. An example snapshot of WT MthK with 4 lipid tails (beige spheres) sticking into the fenestration. **c**. Distribution plots of the fenestration radii for the different channels analyzed with HOLE, as described in Methods. **d**. Time series of the number of lipid tails in the pore during the simulations for WT MthK (left), A90L-MthK and V91F-MthK (right).

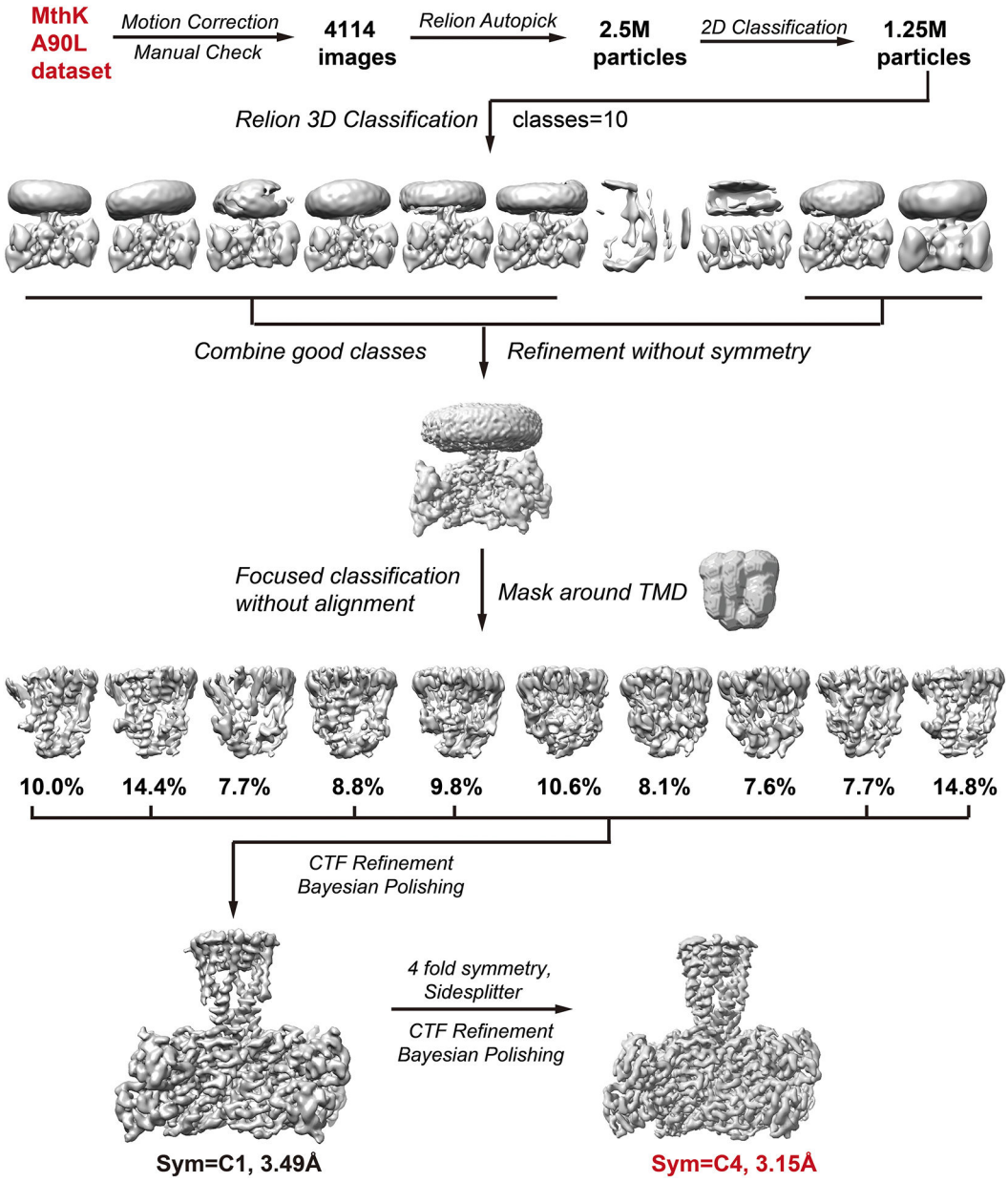

Extended Data Figure 10.

Cryo-EM data processing workflow for the A90L-MthK closed state dataset.

Supplementary Material

Refer to Web version on PubMed Central for supplementary material.

Acknowledgments

We thank L. Yen, M. Kopylov and E. Eng for their support during and data collection at the Simons Electron Microscopy Center and National Resource for Automated Molecular Microscopy located at the New York Structural Biology Center, which is supported by grants from the Simons Foundation (349247), NYSTAR, and the NIH National Institute of General Medical Sciences (GM103310), W. Rice and B. Wang for data collection at NYU Langone Health's Cryo–Electron Microscopy Laboratory (RRID: SCR_019202). The work presented

here was sponsored in part by the NIH GM088352 to CN, the Australian Research Council (DP210102405 and DP2201035501) to TWA, and the National Health and Medical Research Council (APP1141974), National Computational Initiative (dd7), LIEF HPC-GPGPU Facility (LE170100200), DE Shaw Anton 2 (PSCA17045P via NIH RC2GM093307) and the Medical Advances Without Animals Trust to TWA and EF.

Data availability

The maps have been deposited in the Electron Microscopy Data Bank (EMDB) under accession codes (Blocker-free closed MthK: 9405, TPeA-bound closed MthK: 9406, bbTBA-bound closed MthK: 9407, Blocker-free closed A90L MthK: 27459, TPeA-bound closed A88F MthK: 29605). Atomic coordinates for the three structures have been deposited in the Protein Data Bank (PDB) with accession codes 5BKI, 5BKJ, 5BKK, 8DJB, and 8FZ7 respectively. Raw stopped-flow fluorescence quenching traces are available from the corresponding authors upon request.

References

1. Hille B Ion Channels of Excitable Membranes. 3rd edn, (Sinauer Associates, Inc., 2001).
2. Latorre R, Oberhauser A, Labarca P & Alvarez O Varieties of calcium-activated potassium channels. Annu Rev Physiol 51, 385–399, doi:10.1146/annurev.ph.51.030189.002125 (1989). [PubMed: 2653189]
3. McManus OB Calcium-activated potassium channels: regulation by calcium. J Bioenerg Biomembr 23, 537–560 (1991). [PubMed: 1917908]
4. Bailey CS, Moldenhauer HJ, Park SM, Keros S & Meredith AL KCNMA1-linked channelopathy. J Gen Physiol 151, 1173–1189, doi:10.1085/jgp.201912457 (2019). [PubMed: 31427379]
5. Hite RK, Tao X & MacKinnon R Structural basis for gating the high-conductance Ca(2+)-activated K(+) channel. Nature 541, 52–57, doi:10.1038/nature20775 (2017). [PubMed: 27974801]
6. Tao X, Hite RK & MacKinnon R Cryo-EM structure of the open high-conductance Ca(2+)-activated K(+) channel. Nature 541, 46–51, doi:10.1038/nature20608 (2017). [PubMed: 27974795]
7. Tao X & MacKinnon R Molecular structures of the human Slo1 K(+) channel in complex with beta4. Elife 8, doi:10.7554/eLife.51409 (2019).
8. Li W & Aldrich RW State-dependent block of BK channels by synthesized shaker ball peptides. J Gen Physiol 128, 423–441 (2006). [PubMed: 16966472]
9. Zhou Y, Yang H, Cui J & Lingle CJ Threading the biophysics of mammalian Slo1 channels onto structures of an invertebrate Slo1 channel. J Gen Physiol 149, 985–1007, doi:10.1085/jgp.201711845 (2017). [PubMed: 29025867]
10. Tang QY, Zeng XH & Lingle CJ Closed-channel block of BK potassium channels by bbTBA requires partial activation. J Gen Physiol 134, 409–436, doi:jgp.200910251 [pii] 10.1085/jgp.200910251 (2009). [PubMed: 19858359]
11. Wilkens CM & Aldrich RW State-independent block of BK channels by an intracellular quaternary ammonium. J Gen Physiol 128, 347–364 (2006). [PubMed: 16940557]
12. Fan C et al. Ball-and-chain inactivation in a calcium-gated potassium channel. Nature 580, 288–293, doi:10.1038/s41586-020-2116-0 (2020). [PubMed: 32269335]
13. Jiang Y et al. The open pore conformation of potassium channels. Nature 417, 523–526 (2002). [PubMed: 12037560]
14. Jiang Y et al. Crystal structure and mechanism of a calcium-gated potassium channel. Nature 417, 515–522 (2002). [PubMed: 12037559]
15. Ye S, Li Y & Jiang Y Novel insights into K+ selectivity from high-resolution structures of an open K+ channel pore. Nat Struct Mol Biol 17, 1019–1023, doi:nsmb.1865 [pii] 10.1038/nsmb.1865 (2010). [PubMed: 20676101]
16. Jiang Y, Pico A, Cadene M, Chait BT & MacKinnon R Structure of the RCK domain from the E. coli K+ channel and demonstration of its presence in the human BK channel. Neuron 29, 593–601, doi:S0896–6273(01)00236–7 [pii] (2001). [PubMed: 11301020]

17. Yuan P, Leonetti MD, Pico AR, Hsiung Y & MacKinnon R Structure of the human BK channel Ca2+-activation apparatus at 3.0 A resolution. Science 329, 182–186, doi:science.1190414 [pii] 10.1126/science.1190414 (2010). [PubMed: 20508092]
18. Dong J, Shi N, Berke I, Chen L & Jiang Y Structures of the MthK RCK domain and the effect of Ca2+ on gating ring stability. J Biol Chem 280, 41716–41724 (2005). [PubMed: 16227203]
19. Wu Y, Yang Y, Ye S & Jiang Y Structure of the gating ring from the human large-conductance Ca(2+)-gated K(+) channel. Nature 466, 393–397, doi:nature09252 [pii] 10.1038/nature09252 (2010). [PubMed: 20574420]
20. Posson DJ, McCoy JG & Nimigean CM The voltage-dependent gate in MthK potassium channels is located at the selectivity filter. Nat Struct Mol Biol 20, 159–166, doi:nsmb.2473 [pii] 10.1038/nsmb.2473 (2013). [PubMed: 23262489]
21. Posson DJ, Rusinova R, Andersen OS & Nimigean CM Calcium ions open a selectivity filter gate during activation of the MthK potassium channel. Nat Commun 6, 8342, doi:10.1038/ncomms9342 (2015). [PubMed: 26395539]
22. Choi KL, Mossman C, Aube J & Yellen G The internal quaternary ammonium receptor site of Shaker potassium channels. Neuron 10, 533–541 (1993). [PubMed: 8461140]
23. Armstrong CM Time course of TEA(+)-induced anomalous rectification in squid giant axons. J Gen Physiol 50, 491–503 (1966). [PubMed: 11526842]
24. Armstrong CM Inactivation of the potassium conductance and related phenomena caused by quaternary ammonium ion injection in squid axons. J Gen Physiol 54, 553–575, doi:10.1085/jgp.54.5.553 (1969). [PubMed: 5346528]
25. Armstrong CM Interaction of tetraethylammonium ion derivatives with the potassium channels of giant axons. J Gen Physiol 58, 413–437 (1971). [PubMed: 5112659]
26. Armstrong CM & Hille B The inner quaternary ammonium ion receptor in potassium channels of the node of Ranvier. J Gen Physiol 59, 388–400 (1972). [PubMed: 4112955]
27. Choi KL, Aldrich RW & Yellen G Tetraethylammonium blockade distinguishes two inactivation mechanisms in voltage-activated K+ channels. Proc Natl Acad Sci U S A 88, 5092–5095 (1991). [PubMed: 2052588]
28. Baukrowitz T & Yellen G Two functionally distinct subsites for the binding of internal blockers to the pore of voltage-activated K+ channels. Proc Natl Acad Sci U S A 93, 13357–13361 (1996). [PubMed: 8917595]
29. Baukrowitz T & Yellen G Use-dependent blockers and exit rate of the last ion from the multi-ion pore of a K+ channel. Science 271, 653–656 (1996). [PubMed: 8571129]
30. Li W & Aldrich RW Unique inner pore properties of BK channels revealed by quaternary ammonium block. J Gen Physiol 124, 43–57, doi:10.1085/jgp.200409067 (2004). [PubMed: 15197222]
31. Lenaeus MJ, Vamvouka M, Focia PJ & Gross A Structural basis of TEA blockade in a model potassium channel. Nat Struct Mol Biol 12, 454–459 (2005). [PubMed: 15852022]
32. Faraldo-Gomez JD et al. Mechanism of intracellular block of the KcsA K+ channel by tetrabutylammonium: insights from X-ray crystallography, electrophysiology and replica-exchange molecular dynamics simulations. J Mol Biol 365, 649–662 (2007). [PubMed: 17070844]
33. Zhou Y & MacKinnon R The occupancy of ions in the K+ selectivity filter: charge balance and coupling of ion binding to a protein conformational change underlie high conduction rates. J Mol Biol 333, 965–975 (2003). [PubMed: 14583193]
34. Lenaeus MJ, Burdette D, Wagner T, Focia PJ & Gross A Structures of KcsA in complex with symmetrical quaternary ammonium compounds reveal a hydrophobic binding site. Biochemistry 53, 5365–5373, doi:10.1021/bi500525s (2014). [PubMed: 25093676]
35. Cuello LG et al. Structural basis for the coupling between activation and inactivation gates in K(+) channels. Nature 466, 272–275, doi:nature09136 [pii] 10.1038/nature09136 (2010). [PubMed: 20613845]
36. Cuello LG, Jogini V, Cortes DM & Perozo E Structural mechanism of C-type inactivation in K(+) channels. Nature 466, 203–208, doi:nature09153 [pii] 10.1038/nature09153 (2010). [PubMed: 20613835]

37. Bouchard G, Carrupt PA, Testa B, Gobry V & Girault HH The apparent lipophilicity of quaternary ammonium ions is influenced by galvani potential difference, not ion-pairing: a cyclic voltammetry study. Pharm Res 18, 702–708, doi:10.1023/a:1011001914685 (2001). [PubMed: 11465429]
38. Emsley P & Cowtan K Coot: model-building tools for molecular graphics. Acta Crystallogr D Biol Crystallogr 60, 2126–2132 (2004). [PubMed: 15572765]
39. Posson DJ, Rusinova R, Andersen OS & Nimigean CM Stopped-Flow Fluorometric Ion Flux Assay for Ligand-Gated Ion Channel Studies. Methods Mol Biol 1684, 223–235, doi:10.1007/978-1-4939-7362-0_17 (2018). [PubMed: 29058195]
40. Shi N, Zeng W, Ye S, Li Y & Jiang Y Crucial points within the pore as determinants of K(+) channel conductance and gating. J Mol Biol 411, 27–35, doi:10.1016/j.jmb.2011.04.058 (2011). [PubMed: 21554888]
41. Anishkin A, Akitake B, Kamaraju K, Chiang CS & Sukharev S Hydration properties of mechanosensitive channel pores define the energetics of gating. J Phys Condens Matter 22, 454120, doi:10.1088/0953-8984/22/45/454120 (2010). [PubMed: 21339607]
42. Beckstein O & Sansom MS Liquid-vapor oscillations of water in hydrophobic nanopores. Proc Natl Acad Sci U S A 100, 7063–7068, doi:10.1073/pnas.1136844100 (2003). [PubMed: 12740433]
43. Beckstein O & Sansom MS A hydrophobic gate in an ion channel: the closed state of the nicotinic acetylcholine receptor. Phys Biol 3, 147–159, doi:10.1088/1478-3975/3/2/007 (2006). [PubMed: 16829701]
44. del Camino D & Yellen G Tight steric closure at the intracellular activation gate of a voltage-gated K(+) channel. Neuron 32, 649–656 (2001). [PubMed: 11719205]
45. Liu Y, Holmgren M, Jurman ME & Yellen G Gated access to the pore of a voltage-dependent K+ channel. Neuron 19, 175–184 (1997). [PubMed: 9247273]
46. Holmgren M, Smith PL & Yellen G Trapping of organic blockers by closing of voltage-dependent K+ channels: evidence for a trap door mechanism of activation gating. J Gen Physiol 109, 527–535 (1997). [PubMed: 9154902]
47. Jia Z, Yazdani M, Zhang G, Cui J & Chen J Hydrophobic gating in BK channels. Nat Commun 9, 3408, doi:10.1038/s41467-018-05970-3 (2018). [PubMed: 30143620]
48. Dopico AM & Bukiya AN Lipid regulation of BK channel function. Front Physiol 5, 312, doi:10.3389/fphys.2014.00312 (2014). [PubMed: 25202277]
49. Tian Y et al. Atomic determinants of BK channel activation by polyunsaturated fatty acids. Proc Natl Acad Sci U S A 113, 13905–13910, doi:10.1073/pnas.1615562113 (2016). [PubMed: 27849612]
50. Yuan C, O'Connell RJ, Jacob RF, Mason RP & Treistman SN Regulation of the gating of BKCa channel by lipid bilayer thickness. J Biol Chem 282, 7276–7286, doi:10.1074/jbc.M607593200 (2007). [PubMed: 17209047]
51. Vaithianathan T et al. Direct regulation of BK channels by phosphatidylinositol 4,5-bisphosphate as a novel signaling pathway. J Gen Physiol 132, 13–28, doi:10.1085/jgp.200709913 (2008). [PubMed: 18562499]
52. Yohannan S, Hu Y & Zhou Y Crystallographic study of the tetrabutylammonium block to the KcsA K+ channel. J Mol Biol 366, 806–814 (2007). [PubMed: 17196615]
53. Boiteux C, Posson DJ, Allen TW & Nimigean CM Selectivity filter ion binding affinity determines inactivation in a potassium channel. Proc Natl Acad Sci U S A 117, 29968–29978, doi:10.1073/pnas.2009624117 (2020). [PubMed: 33154158]
54. Gamal El-Din TM, Lenaeus MJ, Zheng N & Catterall WA Fenestrations control resting-state block of a voltage-gated sodium channel. Proc Natl Acad Sci U S A 115, 13111–13116, doi:10.1073/pnas.1814928115 (2018). [PubMed: 30518562]
55. Yan Z et al. Structure of the Nav1.4-beta1 Complex from Electric Eel. Cell 170, 470–482 e411, doi:10.1016/j.cell.2017.06.039 (2017). [PubMed: 28735751]
56. Boiteux C et al. Local anesthetic and antiepileptic drug access and binding to a bacterial voltage-gated sodium channel. Proc Natl Acad Sci U S A 111, 13057–13062, doi:10.1073/pnas.1408710111 (2014). [PubMed: 25136136]

57. Zhao Y et al. Molecular Basis for Ligand Modulation of a Mammalian Voltage-Gated Ca(2+) Channel. Cell 177, 1495–1506 e1412, doi:10.1016/j.cell.2019.04.043 (2019). [PubMed: 31150622]
58. Wu J et al. Structure of the voltage-gated calcium channel Cav1.1 complex. Science 350, aad2395, doi:10.1126/science.aad2395 (2015). [PubMed: 26680202]
59. Dong YY et al. K2P channel gating mechanisms revealed by structures of TREK-2 and a complex with Prozac. Science 347, 1256–1259, doi:10.1126/science.1261512 (2015). [PubMed: 25766236]
60. Chen Y et al. Structure of the STRA6 receptor for retinol uptake. Science 353, doi:10.1126/science.aad8266 (2016).
61. Jorgensen C et al. Lateral Fenestrations in K(+)-Channels Explored Using Molecular Dynamics Simulations. Mol Pharm 13, 2263–2273, doi:10.1021/acs.molpharmaceut.5b00942 (2016). [PubMed: 27173896]
62. Smith FJ, Pau VP, Cingolani G & Rothberg BS Structural basis of allosteric interactions among Ca2+-binding sites in a K+ channel RCK domain. Nat Commun 4, 2621, doi:10.1038/ncomms3621 (2013). [PubMed: 24126388]
63. Suloway C et al. Automated molecular microscopy: the new Leginon system. Journal of structural biology 151, 41–60, doi:10.1016/j.jsb.2005.03.010 (2005). [PubMed: 15890530]
64. Zivanov J et al. RELION-3: new tools for automated high-resolution cryo-EM structure determination. bioRxiv, doi:10.1101/421123 (2018).
65. Zivanov J, Nakane T & Scheres SHW A Bayesian approach to beam-induced motion correction in cryo-EM single-particle analysis. IUCrJ 6, 5–17, doi:10.1107/S205225251801463X (2019).
66. Rohou A & Grigorieff N CTFFIND4: Fast and accurate defocus estimation from electron micrographs. Journal of structural biology 192, 216–221, doi:10.1016/j.jsb.2015.08.008 (2015). [PubMed: 26278980]
67. Pettersen EF et al. UCSF Chimera--a visualization system for exploratory research and analysis. J Comput Chem 25, 1605–1612, doi:10.1002/jcc.20084 (2004). [PubMed: 15264254]
68. Emsley P, Lohkamp B, Scott WG & Cowtan K Features and development of Coot. Acta Crystallogr D Biol Crystallogr 66, 486–501, doi:10.1107/S0907444910007493 (2010). [PubMed: 20383002]
69. Afonine PV et al. Real-space refinement in PHENIX for cryo-EM and crystallography. Acta Crystallogr D Struct Biol 74, 531–544, doi:10.1107/S2059798318006551 (2018). [PubMed: 29872004]
70. Brooks BR et al. CHARMM: the biomolecular simulation program. J. Comput. Chem 30, 1545–1614 (2009). [PubMed: 19444816]
71. Phillips JC et al. Scalable molecular dynamics with NAMD. Journal of computational chemistry 26, 1781–1802 (2005). [PubMed: 16222654]
72. Shaw DE et al. in Proceedings of the international conference for high performance computing, networking, storage and analysis. 41–53 (IEEE Press).
73. Klauda JB et al. Update of the CHARMM all-atom additive force field for lipids: validation on six lipid types. The journal of physical chemistry B 114, 7830–7843 (2010). [PubMed: 20496934]
74. MacKerell AD Jr et al. All-atom empirical potential for molecular modeling and dynamics studies of proteins. The journal of physical chemistry B 102, 3586–3616 (1998). [PubMed: 24889800]
75. MacKerell AD, Feig M & Brooks CL Extending the treatment of backbone energetics in protein force fields: Limitations of gas-phase quantum mechanics in reproducing protein conformational distributions in molecular dynamics simulations. J. Comput. Chem 25, 1400–1415 (2004). [PubMed: 15185334]
76. Noskov SY, Berneche S & Roux B Control of ion selectivity in potassium channels by electrostatic and dynamic properties of carbonyl ligands. Nature 431, 830–834 (2004). [PubMed: 15483608]
77. Vanommeslaeghe K et al. CHARMM general force field: A force field for drug-like molecules compatible with the CHARMM all-atom additive biological force fields. J Comput Chem 31, 671–690, doi:10.1002/jcc.21367 (2010). [PubMed: 19575467]
78. Andersen HC Molecular dynamics simulations at constant pressure and/or temperature. The Journal of chemical physics 72, 2384–2393 (1980).

79. Feller SE, Zhang Y, Pastor RW & Brooks BR Constant pressure molecular dynamics simulation: the Langevin piston method. The Journal of chemical physics 103, 4613–4621 (1995).
80. Martyna GJ, Tobias DJ & Klein ML Constant pressure molecular dynamics algorithms. The Journal of Chemical Physics 101, 4177–4189 (1994).
81. Nosé S A unified formulation of the constant temperature molecular dynamics methods. The Journal of chemical physics 81, 511–519 (1984).
82. Hoover WG Canonical dynamics: equilibrium phase-space distributions. Physical review A 31, 1695 (1985).
83. Andersen HC Rattle: A "velocity" version of the shake algorithm for molecular dynamics calculations. J. Comput. Phys 52, 24–34, doi:10.1016/0021-9991(83)90014-1 (1983).
84. Darden T, York D & Pedersen L Particle mesh Ewald: An N-log(N) method for Ewald sums in large systems. J. Chem. Phys 98, 10089 (1993).
85. Shan Y, Klepeis JL, Eastwood MP, Dror RO & Shaw DE Gaussian split Ewald: A fast Ewald mesh method for molecular simulation. The Journal of chemical physics 122, 054101 (2005).
86. Torrie GM & Valleau JP Nonphysical sampling distributions in Monte Carlo free-energy estimation: Umbrella sampling. Journal of Computational Physics 23, 187–199, doi:10.1016/0021-9991(77)90121-8 (1977).
87. Kumar S, Rosenberg JM, Bouzida D, Swendsen RH & Kollman PA THE weighted histogram analysis method for free-energy calculations on biomolecules. I. The method. Journal of Computational Chemistry 13, 1011–1021, doi:10.1002/jcc.540130812 (1992).
88. Kumar S, Rosenberg JM, Bouzida D, Swendsen RH & Kollman PA The weighted histogram analysis method for free-energy calculations on biomolecules. I. The method. J Comput Chem 13, 1011–1021 (1992).
89. Allen TW, Andersen OS & Roux B The structure of gramicidin A in a lipid bilayer environment determined using molecular dynamics simulations and solid-state NMR data. J. Am. Chem. Soc 125, 9868–9877 (2003). [PubMed: 12904055]
90. Crouzy S, Woolf TB & Roux B A Molecular Dynamics Study of Gating in Dioxolane- Linked Gramicidin A Channels. Biophys. J 67, 1370–1386 (1994). [PubMed: 7529578]
91. Allen TW, Andersen OS & Roux B Energetics of ion conduction through the gramicidin channel Proc. Nat. Acad. Sci 101 117–122 (2004). [PubMed: 14691245]
92. Roux B, Andersen OS & Allen TW Comment on "Free energy simulations of single and double ion occupancy in gramicidin A" [J. Chem. Phys. 126, 105103 (2007)]. J. Chem. Phys 128 (2008).
93. Hummer G Position-dependent diffusion coefficients and free energies from Bayesian analysis of equilibrium and replica molecular dynamics simulations. New Journal of Physics 7, 34 (2005).
94. Trabuco LG, Villa E, Mitra K, Frank J & Schulten K Flexible fitting of atomic structures into electron microscopy maps using molecular dynamics. Structure 16, 673–683 (2008). [PubMed: 18462672]

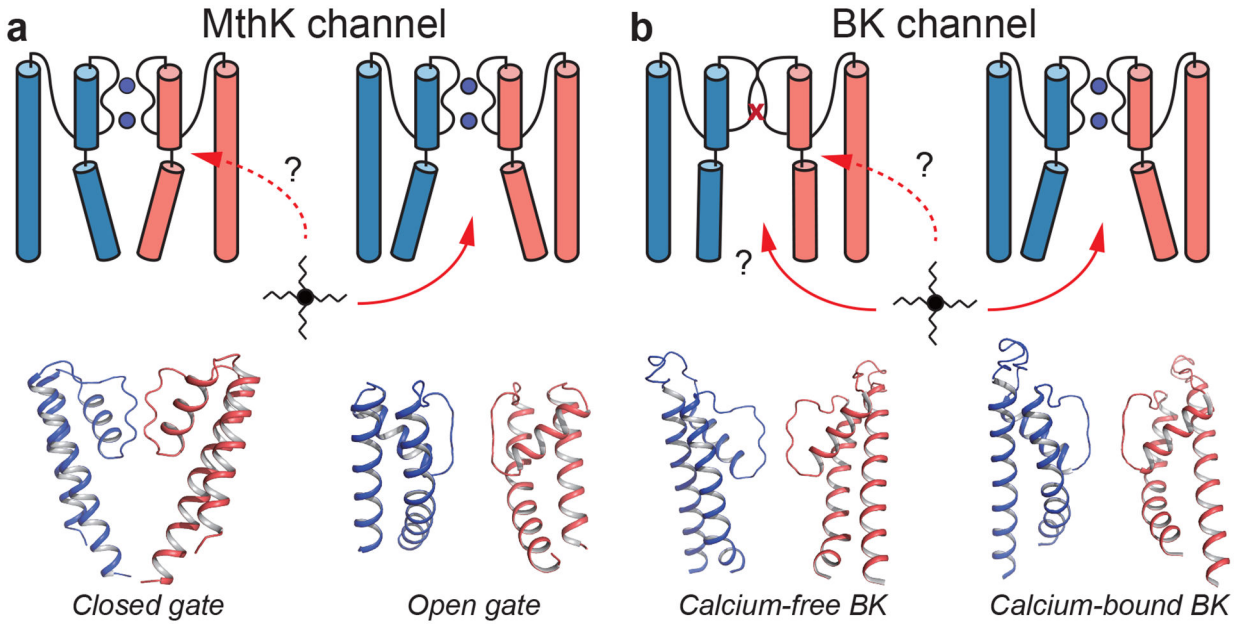

Figure 1. Alternative entry pathways for intracellular quaternary ammonium (QA) blockers in the closed MthK and BK pores.

Schematic cartoons (top panels) indicating that although QA blockers (black molecule) may access the open channel pores via the traditional conduction pathway, the closed channel pores may be entered via either (**a**) a lateral membrane fenestration if the ionic gate is at the bundle crossing as for MthK channels, or (**b**) via the conduction pathway if the gate is at the selectivity filter as is proposed for BK channels. Bottom panels: **a**. Cartoon rendering of MthK channel structures in closed (PDB 6U6D) and open (PDB 3LDC) states. **b**. Cartoon rendering of human BK pore structure in EDTA (PDB 6V3G) and with Ca^{2+} bound (PDB 6V38). Only the pore region of two opposing subunits (blue and red) is shown. Red arrows indicate the access pathways of the intracellular QA blocker to the pore.

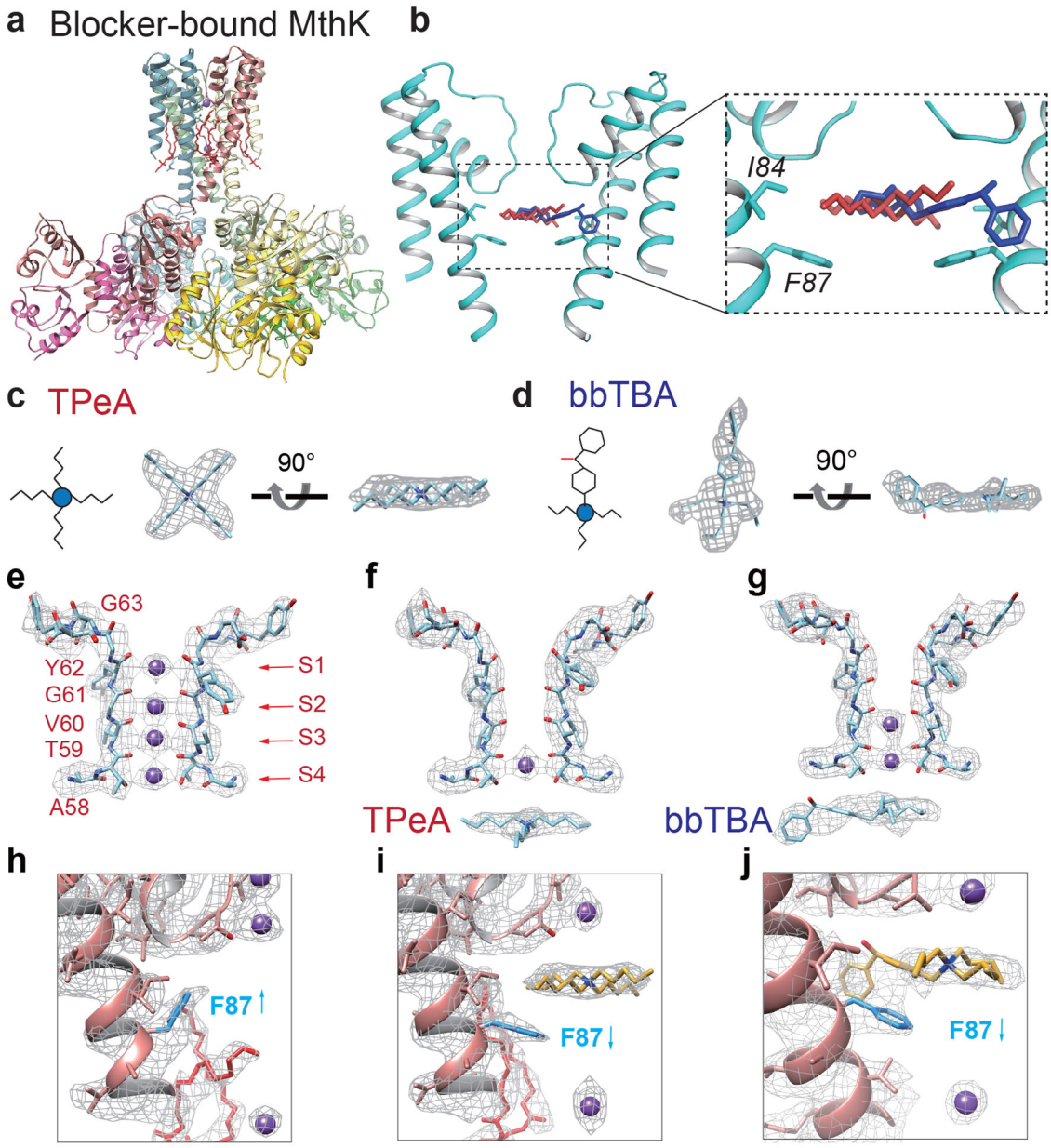

Figure 2. TPeA and bbTBA bind below the selectivity filter and change the K^+ occupancy in closed MthK structures.

a. Overall structure of TPeA-bound MthK. Each subunit is in a different color, lipids in red,. **b**. Binding sites of TpeA and bbTBA in the closed MthK pore under selectivity filter. Structures of MthK-TpeA and MthK-bbTBA are identical and superimposed, with only the pore region of two opposing subunits shown as cyan cartoon. Blockers are shown as red and blue sticks, respectively. Inset expands the dashed rectangle. Residues coordinating the blockers are labeled. Cryo-EM map densities for TpeA (**c**) and bbTBA (**d**). Density is grey mesh, and the model cyan sticks. Cartoon renditions of the blockers are also shown with ammonium in blue and oxygen in red(**c-d**). Selectivity filter with four K^+ densities (grey mesh) in blocker-free closed MthK (**e**), compared to one K^+ in S4 of the TPeA-bound closed MthK (**f**), and two K^+ in S3 and S4 in the bbTBA-bound closed MthK (**g**) structures. K^+ are

shown as purple spheres. Side chain of F87 adopts the (**h**) up conformation in blocker-free, (**i**) down conformation in TPeA-bound and (**j**) down conformation in bbTBA-bound closed MthK. Only one F87 side chain is shown in **j**, with the other 3 shown in Extended Data Fig. 1e.

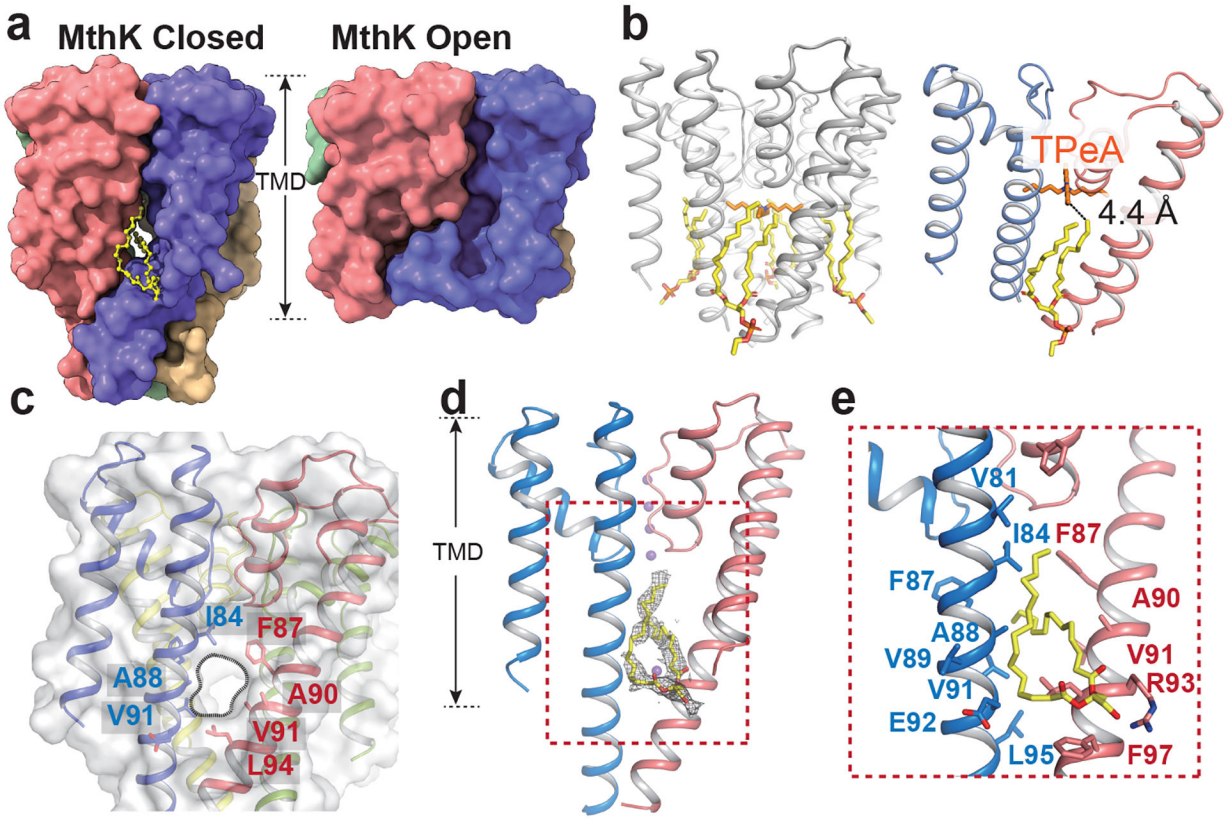

Figure 3. Fenestration and lipid binding in MthK closed structure.

a) MthK closed structure displays lateral fenestrations between two TM2 helices from adjacent subunits. Fenestration was not observed in open MthK as TM2 helix bends up and fills it. The four subunits are in purple, red, green and tan. Lipid is yellow stick. **b**. Left: Cartoon of TPeA-bound closed MthK (grey ribbons), with TPeA in orange and lipids in yellow sticks. Right: 2 adjacent subunits (red and blue cartoon ribbons) of TPeA-bound closed MthK highlighting the through-fenestration lipid coordination of TPeA bound under the selectivity filter**. c**. Fenestration in closed MthK. The four subunits are in transparent surface representation, overlayed with subunits in red, blue, green and yellow ribbon cartoons. Fenestration was contoured by a dashed line, and residues lining it (I84, A88, V91 of one TM2, and F87, A90, V91, L94 of the adjacent TM2) are labeled sticks. **d**. Lipid density (grey mesh) in the MthK fenestration. Lipid sticks are yellow for carbon atoms and red for oxygen atoms. Dashed rectangle is the region of (**d**) expanded in **e**. **e**. Expanded view shows the lipid binding and surrounding residues with the head group interacting with R93 in TM2 (labeled sticks).

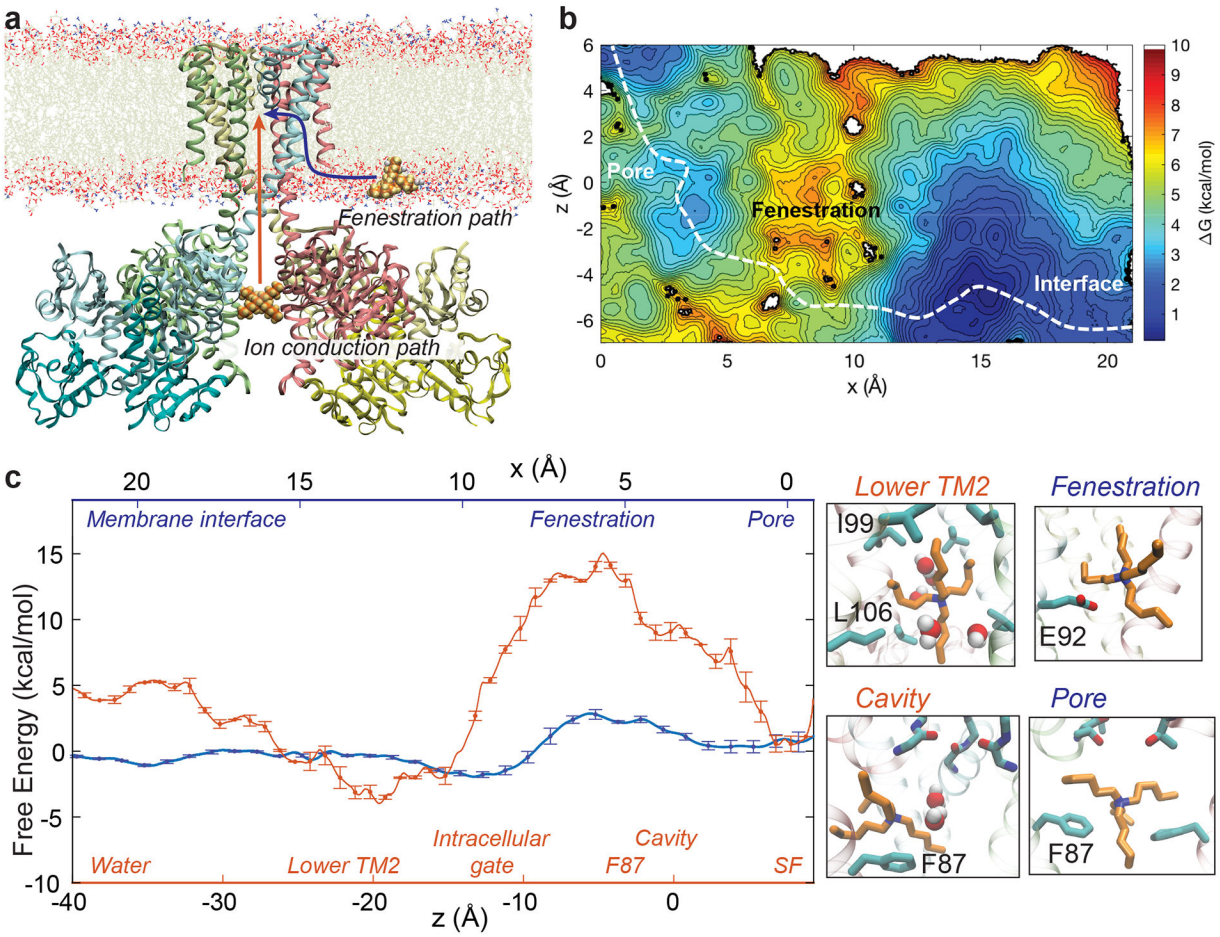

Figure 4. Free energetics of TPeA entry to the closed MthK pore.

a. Closed MthK (ribbon cartoons colored as in Fig. 2a) embedded in a hydrated POPE: POPG (3:1) lipid bilayer (thin sticks) with the two possible paths, via which TPeA (orange space filled model) can enter the MthK pore, indicated by arrows. **b**. 2D free energy map for crossing through the fenestration from the membrane interface into the pore, with the dashed curve indicating the lowest free energy path. **c**. Free energy profile for TPeA entering though the MthK gate (red) and 1D free energy projection for TPeA entering through the fenestration (blue) derived from 2D US. Free energies for these different profiles have been matched in the pore binding site. Gate binding US used 48 independent simulations, whereas fenestration binding 2D US used 291 independent simulations, with final error bars based on n=2 blocks ($\pm\frac{1}{2}$ the difference) following equilibration (see Methods). Insets show TPeA (orange sticks) positioning at the indicated locations throughout the paths. Locations of the intracellular gate, F87 and SF (SF) are indicated on the z axis, and of the membrane interface, fenestration and pore, on the x axis.

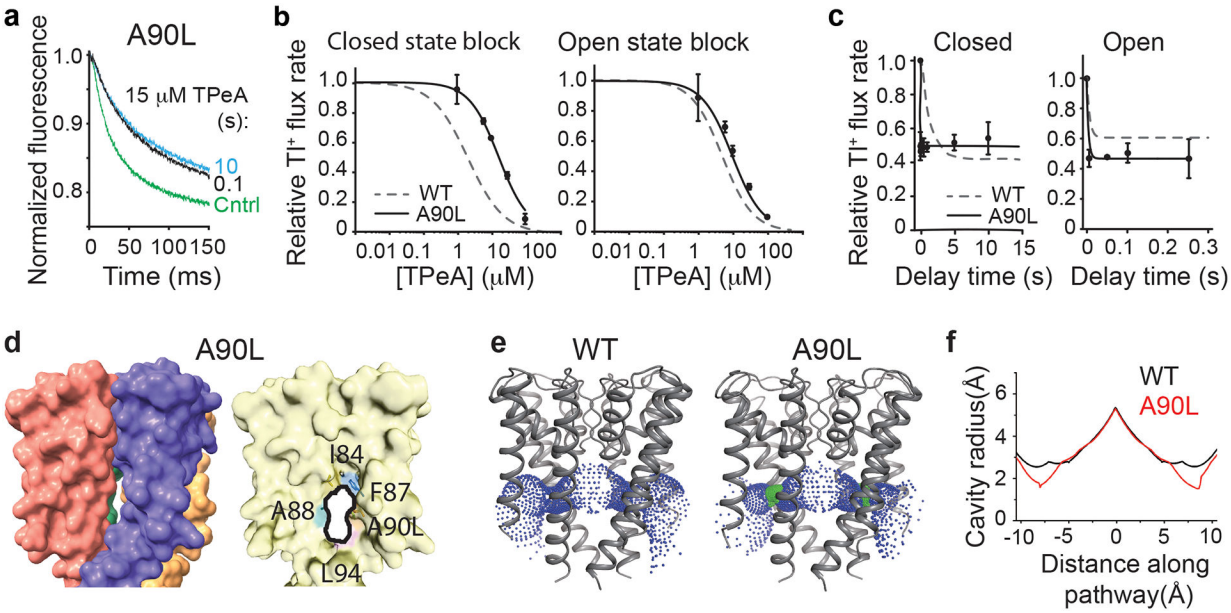

Figure 5. TPeA entry is impeded through the narrower fenestrations of A90L MthK closed.

a. Fluorescence quench traces after incubating MthK A90L-containing liposomes in the absence of Ca^{2+} with 15 μM TPeA for 0.1 (black) and 10 (cyan) s and no blocker control (green) (lines include n=6 technical repeats each). **b**. Dose response plots for closed-state (left) and open-state (right) TPeA block of A90L MthK after 10 s and 100ms incubation, respectively. Solid lines are Hill equation fits with K_D^{closed} = 16.8 ± 2.4 μM, n_H = 1 and K_D^{open} = 9.7 ± 1.7 μM, n_H = 1, n=3 repeats each. The fits for MthK WT (dashed lines) after same blocker incubation times are overlayed (K_D^{closed} = 2.1 ± μM, n_H = 0.84, and K_D^{open} = 5.2 ± μM, n_H = 0.98) (from Posson et al. (2015))[21]. **c**. Relative Tl^+ flux rates as a function of incubation time with 15 μM TPeA from data as in **a** to measure equilibration time for TPeA with closed (left) and open (right) A90L MthK. Solid lines are fits with a first-order exponential decay function. τ_{closed}= 5.6 ± 0.51 ms, and τ_{open}= 0.36 ± 0.04 ms (the block equilibrates within the instrument dead time of 10 ms). n=2 biological replicates. Each biological replicate is the mean of n=6 technical repeats. The dashed lines are equilibration plots for 3 μM TPeA with WT MthK, from Posson et al. (2015))[21]. All data are presented as mean±SD. **d**. Structure of A90L MthK closed state displays lateral fenestrations between two TM2 helices from adjacent subunits, rendered to compare with WT in Fig. 3a (left) and to highlight fenestration size and the residues that line it (right). The introduced leucine sidechain at position 90 faces towards the TM2 of neighboring subunit to decrease fenestration size. **e**. Fenestration calculated using program HOLE indicates a ~1.5 A radius for A90L (green dots indicate only one water molecule can squeeze through the narrowest part of the fenestration). **f**. Plots of the fenestration cavity radius, shown in **e**. The dips in the red graph indicate the narrowest fenestration points of A90L MthK, compared with WT (black).